Bull Volcanol (2007) 69: 281–300
DOI 10.1007/s00445-006-0073-6

RESEARCH ARTICLE

Heather M. N. Wright · Katharine V. Cashman · Mauro Rosi · Raffaello Cioni

Breadcrust bombs as indicators of Vulcanian eruption dynamics at Guagua Pichincha volcano, Ecuador

Received: 2 May 2005 / Accepted: 24 March 2006 / Published online: 7 July 2006

Abstract Vulcanian eruptions are common at many volcanoes around the world. Vulcanian activity occurs as either isolated sequences of eruptions or as precursors to sustained explosive events and is interpreted as clearing of shallow plugs from volcanic conduits. Breadcrust bombs characteristic of Vulcanian eruptions represent samples of different parts of these plugs and preserve information that can be used to infer parameters of pre-eruption magma ascent. The morphology and preserved volatile contents of breadcrust bombs erupted in 1999 from Guagua Pichincha volcano, Ecuador, thus allow us to constrain the physical processes responsible for Vulcanian eruption sequences of this volcano. Morphologically, breadcrust bombs differ in the thickness of glassy surface rinds and in the orientation and density of crack networks. Thick rinds fracture to create deep, widely spaced cracks that form large rectangular domains of surface crust. In contrast, thin rinds form polygonal networks of closely spaced shallow cracks. Rind thickness, in turn, is inversely correlated with matrix glass water content in the rind. Assuming that all rinds cooled at the same rate, this correlation suggests increasing bubble nucleation delay times with decreasing pre-fragmentation water content of the melt. A critical bubble nucleation threshold of 0.4–0.9 wt% water exists, below which bubble nucleation does not occur and resultant bombs are dense. At pre-fragmentation melt H_2O contents of >~0.9 wt%, only glassy rinds are dense and bomb interiors vesiculate after fragmentation. For matrix glass H_2O contents of ≥1.4 wt%, rinds are thin and vesicular instead of thick and non-vesicular. A maximum measured H_2O content of 3.1 wt% establishes the maximum pressure (63 MPa) and depth (2.5 km) of magma that may have been tapped during a single eruptive event. More common H_2O contents of ≤1.5 wt% suggest that most eruptions involved evacuation of ≤1.5 km of the conduit. As we expect that substantial overpressures existed in the conduit prior to eruption, these depth estimates based on magmastatic pressure are maxima. Moreover, the presence of measurable CO_2 (≤17 ppm) in quenched glass of highly degassed magma is inconsistent with simple models of either open- or closed-system degassing, and leads us instead to suggest re-equilibration of the melt with gas derived from a deeper magmatic source. Together, these observations suggest a model for the repeated Vulcanian eruptions that includes (1) evacuation of the shallow conduit during an individual eruption, (2) depressurization of magma remaining in the conduit accompanied by open-system degassing through permeable bubble networks, (3) rapid conduit re-filling, and (4) dome formation prior to the subsequent explosion. An important part of this process is densification of upper conduit magma to allow repressurization between explosions. At a critical overpressure, trapped pressurized gas fragments the nascent impermeable cap to repeat the process.

Keywords Breadcrust bomb · Vulcanian · Water content · Degassing · Permeability

Editorial responsibility: J. White

H. M. N. Wright (✉) · K. V. Cashman
Department of Geological Sciences, University of Oregon,
Eugene, OR 97403-1272, USA
e-mail: wrighthm@alumni.whitman.edu
Tel.: +1-541-3465987
Fax: +1-541-3464692

M. Rosi
Dipartimento Scienze della Terra, University Pisa,
Via S. Maria 53,
I-56126 Pisa, Italy

R. Cioni
Dipartimento Scienze della Terra, University Cagliari,
Via Trentino 51,
I-09124 Cagliari, Italy

Introduction

Vulcanian eruptions are short (seconds to minutes), violent outbursts that eject relatively small volumes of magma (<1 km^3; Morrissey and Mastin 2000). These eruptions may occur either as a series of discrete events or as precursors to sustained subplinian or Plinian eruptions

(e.g., Nairn and Self 1978; Druitt et al. 2002). High pyroclast ejection velocities during individual events (≤400 m/s; Morrissey and Mastin 2000) reflect high mass eruption rates that result from gas pressurization within the conduit (Chouet et al. 1994; Cruz and Chouet 1997; Arciniega-Ceballos et al. 1999). Resultant volcanic plumes can reach up to several km in height for a single eruption or up to 20 km for repeated eruptions and produce moderately dispersed deposits (Morrissey and Mastin 2000). Vulcanian eruptions may generate pyroclastic avalanches, pyroclastic flows, block and ash flows, distal, thin ash falls, and proximal, often breadcrusted ballistic blocks (e.g., Vougioukalakis 1995). Of these, breadcrusted clasts are particularly characteristic of Vulcanian eruptive styles.

A long-standing question about Vulcanian eruptions is whether the overpressures required to drive these explosions result solely from the accumulation of magmatic volatiles beneath an impermeable cap (e.g., Turcotte et al. 1990; Fagents and Wilson 1993; Clarke et al. 2002) or whether they require interaction of magma with external water (e.g., Schmincke et al. 1990; Capra et al. 1998). Early estimates of ballistic block ejection velocities of ≤600 m/s (Fudali and Melson 1972; Self et al. 1979) were too high to be produced by magmatic gases alone, thus involvement of external water was invoked to explain particularly violent events (Melson and Saenz 1974; Self et al. 1979; Fisher and Schmincke 1984; Francis 1993; Woods 1995). However, new models of ballistic behavior reduce these velocity estimates by half, although gas velocity itself may be higher than ballistic ejection velocity (Fagents and Wilson 1993; Morrissey and Mastin 2000). These models require overpressures of only ~10–20 MPa, overpressures achievable by a combination of decompression-induced degassing, groundmass crystallization, and permeable gas migration beneath an impermeable barrier (Nakada et al. 1995; Sparks 1997; Stix et al. 1997; Barmin et al. 2002; Melnik and Sparks 2002; Edmonds et al. 2003).

Like the explosions that produce them, breadcrust bombs have been variably interpreted to reflect either quenching of magma by external water (e.g., Fisher and Schmincke 1984; Francis 1993) or delayed vesiculation of partially degassed magma (e.g., Turcotte et al. 1990; Hoblitt and Harmon 1993; Yamagishi and Feebrey 1994). Studies that invoke a magmatic origin for this bomb type vary in explanations of the mechanism by which breadcrusting occurs. Exterior cracking (and resultant crack patterns) may occur (1) as a result of interior expansion of a bomb with a quenched exterior rind, (2) in response to thermal contraction of the outer surface, or (3) from stresses applied during impact. In his original study of the eponymous eruptions of Vulcano, Italy, Walker (1969, 1982) defined three basic bomb styles: (1) dense blocks that were hot upon impact but did not expand, (2) blocks with thick quenched rinds and limited expansion, and (3) highly expanded blocks with thin glassy crusts and broad, shallow cracks. He explained these differences in clast morphology by differences in clast cooling times and resultant differences in magma viscosity. More recently, Hoblitt and Harmon (1993) used measured H_2O contents in glassy rinds to suggest that breadcrust bombs produced by disruption of the cryptodome at Mount St. Helens, WA, 1980, resulted from pre-eruptive magma degassing that produced a sufficient delay in syn-eruptive bubble nucleation to allow rind formation. In a different volcanic setting, Polacci et al. (2001) proposed that breadcrusting of pumiceous clasts produced during the June 15 climactic eruption of Pinatubo volcano, 1991, was promoted by locally high temperatures and lower volatile content. Additionally, Yamagishi and Feebrey (1994) hypothesized that unusual breadcrust bombs with vesicular outer rinds and dense interiors from Tokachidake volcano, Japan, reflect pre-eruptive magma degassing along cracks beneath an impermeable cap. Although different in specifics, all three recent models for vulcanian breadcrust-bomb formation require some amount of pre-eruptive volatile loss.

What conditions promote the pre-eruptive degassing and pressurization apparently required to produce Vulcanian explosions? Despite the frequency of Vulcanian eruptions at volcanoes with actively growing lava domes of intermediate to silicic compositions, and the real hazard they pose, the physical processes responsible for this type of activity are poorly understood. In particular, there are few constraints on processes that modulate the observed cyclic behavior (an exception being the well-documented events at Soufrière Hills Volcano, Montserrat, e.g., Druitt et al. 2002; Edmonds et al. 2003; Formenti et al. 2003). Here we use abundant and variably breadcrusted bombs produced during activity at Guagua Pichincha volcano, Ecuador, in late 1999 to examine processes responsible for Vulcanian activity of this system. Furthermore, the characteristic association of breadcrust bombs with Vulcanian eruptions (e.g., Morrissey and Mastin 2000) suggests that a study of bomb formation should provide important insight into the general nature of Vulcanian explosive activity.

The 1999 eruptions of Guagua Pichincha volcano

Guagua Pichincha is a dacitic stratovolcano located 12 km west of Quito, Ecuador (Fig. 1), in the Central Volcanic Zone of the South American Andes. It has been active for the past 50,000 years, evolving into its current eruptive phase almost 12,000 years ago. Early phases were dominated by effusive eruptions that formed the lava cone, slope failure and formation of a breached amphitheater, and subsequent effusive and explosive eruptions from the central vent in the amphitheater (Barberi et al. 1992). Holocene eruption styles at Guagua Pichincha volcano have been dominantly explosive and include phreatic explosions, dome growth and collapse, Vulcanian eruptions, Plinian ash falls, and pyroclastic flows (Barberi et al. 1992; Hall 2001).

The most recent eruptive period, described by Villagomez (2000), began in 1981 with a period of phreatic activity that included gas and ash explosions and an increase in fumarole gas emission. A second phase of activity initiated in August 1998 with the onset of larger phreatic eruptions and an increase in the number of hybrid (medium frequency)

Fig. 1 Map of major volcanoes (*triangles*) and major cities (*squares*) in Ecuador

earthquakes. Phreatic eruptions occurred weekly to daily for approximately one year, expelling mud, gas, and rock fragments from the crater. A third, dominantly magmatic phase of the eruption began on September 26, 1999, with two subplinian and several Vulcanian eruptions and construction and destruction of seven domes between late September and December 1999 (Hall 2001). The first dome emerged on September 28 and persisted until October 5, when it was destroyed by a subplinian eruption, the largest of the eruptive sequence. This eruption was followed by a second subplinian eruption on October 7th and a long period of dome growth without accompanying explosions between October 7th and November 15th, the first Vulcanian event. Vulcanian dome-destroying eruptions then occurred at approximately one-week intervals through December; frequent LP seismicity and infrequent VT seismicity accompanied explosions and eruptions throughout this period (Fig. 2). Each Vulcanian eruption was short, accompanied by several seismic explosion signals, involved a small volume of magma, and produced an ash cloud ≤10 km high (Hall 2001). For clarification, we will use the term explosion to refer to explosion seismic signals, eruption to denote ejection of material from the vent, and fragmentation to represent the transition from a continuous melt or solid phase containing bubbles to a continuous gas phase containing parcels of bubbly melt/solid (Cashman et al. 2000).

Deposits from Vulcanian eruptions at Guagua Pichincha include a thin fine ash bed, channelized deposits of block and ash flows that traveled several kilometers from the vent down the breached western flank of the volcano, and abundant ballistic blocks and bombs that cover the surface of Guagua Pichincha's summit crater. Ballistics range up to ~1.5 m in diameter; most of the clasts have prismatic faces, but variable surface morphologies (Fig. 3). Dense blocks are abundant and were ejected to greater distances from the vent than bombs with breadcrust morphologies, a result of either a lower angle take-off or higher muzzle velocity of ejection. Breadcrust bombs have surface morphologies that vary in both surface texture (dense glassy or pumiceous) and patterns of crack networks.

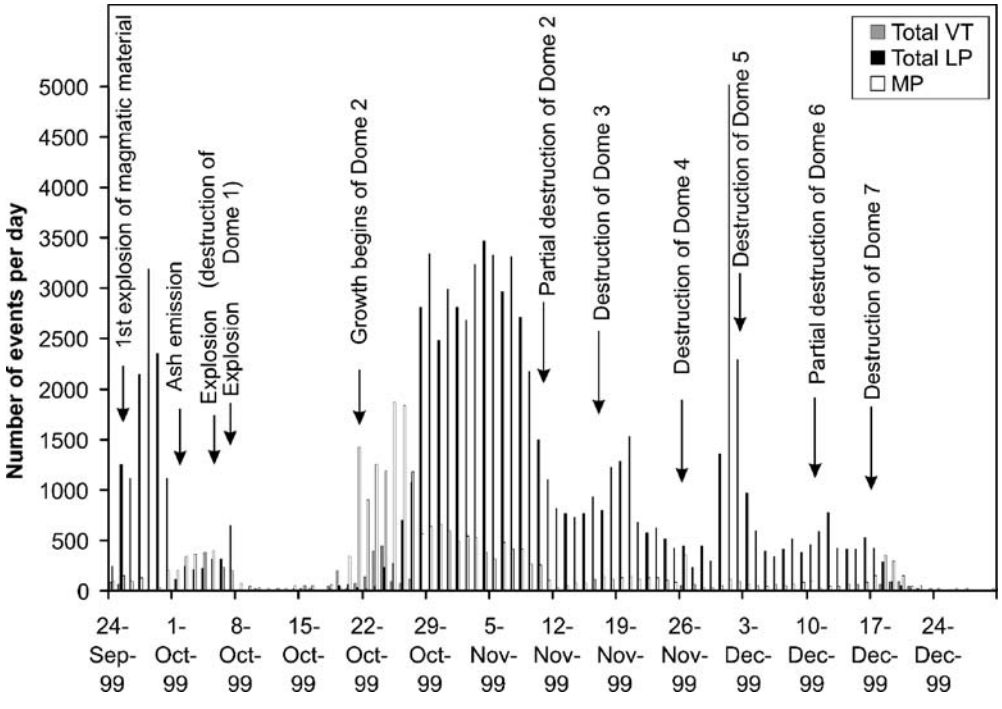

Fig. 2 Eruption sequence at Guagua Pichincha for period 24 Sept-28 Dec 1999; data from Instituto Geofisico, Escuela Politecnica Nacional, Ecuador

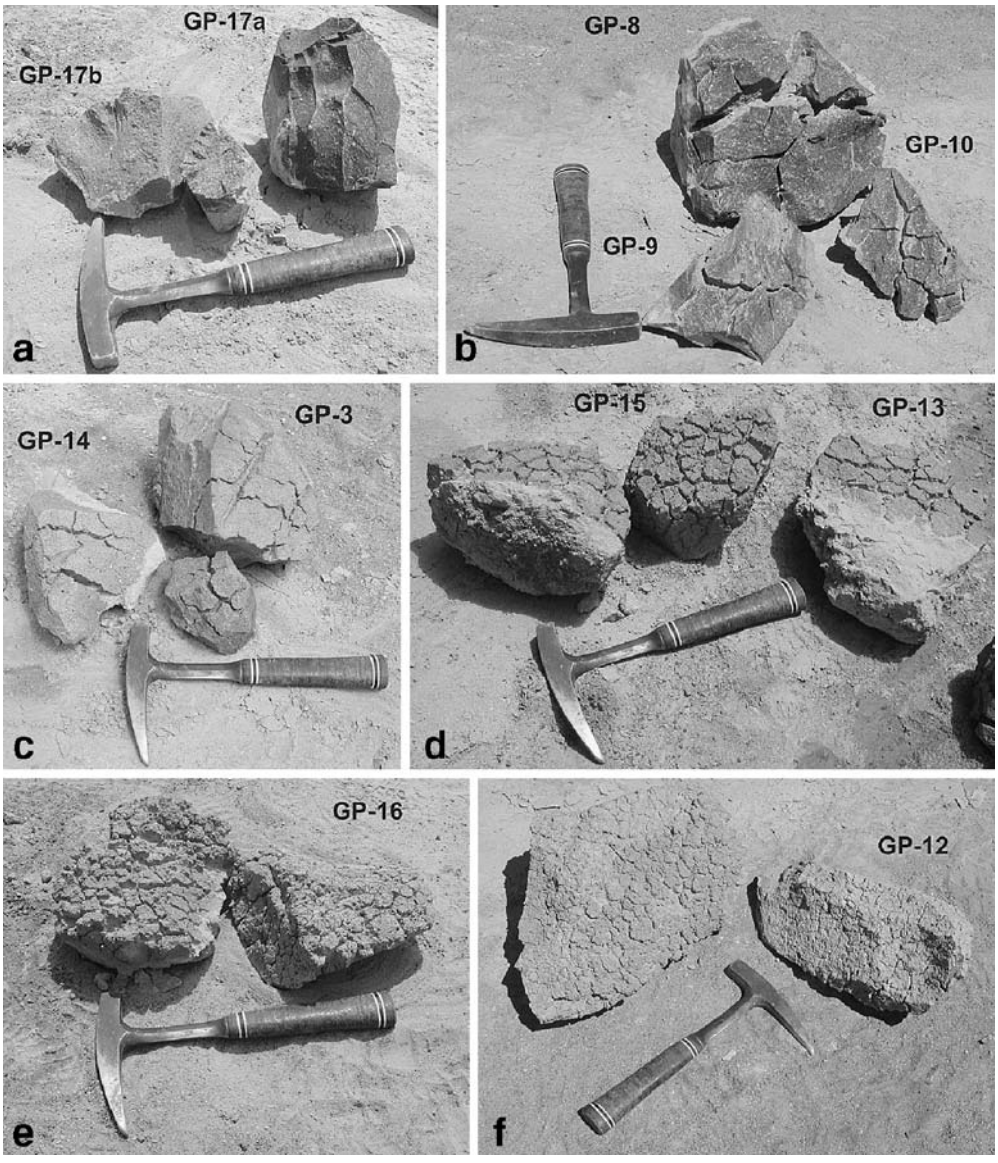

Fig. 3 Volcanic bomb textures at Pichincha volcano (in order of increasing interior vesicularity: **a** dense, non-breadcrusted bombs (*DB*), **b** thick crusted breadcrust bombs with dense, glassy rinds (*TkB*), **c** flow-banded bombs (banding not visible in this picture) with intermediate crack depths (*FIB*), **d**–**f** thinly breadcrusted bombs with shallow cracks and vesicular rinds (*TnB*)

Methods

To explore the relationship between breadcrust bombs and Vulcanian eruptions at Guagua Pichincha, we completed a textural survey of a large number of bombs in the field, classifying them into morphologic groups on the basis of their apparent density and surface characteristics. We then collected 2–3 bombs 7–20 cm in diameter from each class (Fig. 3). Half of these samples are complete bombs with all faces preserved. Because individual Vulcanian eruptions were similar in both duration and magnitude, we assume that a complete sampling of all bomb types on the crater floor represents the full spectrum of bomb types ejected in a single eruption. This assumption is supported by the similarity in bulk composition of all bombs (Table 1). However, we recognize that textural variations might be expected for the products of the November 17th eruptions, which followed a particularly long repose interval, and from the subplinian eruptions of October 5 and 7, which also produced pumiceous fall deposits. We note, however, that no breadcrust bombs were observed in the October 5 pumice fallout bed preserved within the crater.

Crack volume, width, depth, and orientation

To determine the extent to which post-fragmentation bomb expansion is reflected in the surface cracks (breadcrusting), we measured the volume of both the whole clast and the surface cracks for the six samples with completely preserved surfaces. Volumes were determined by water displacement, using Archimedes' principle (Fig. 4a). As the clasts are permeable to water, especially through more vesicular surfaces, we first saturated the samples with water for several days to minimize the effect of water penetration on volume measurements. After completing measurements on whole bombs, we filled the cracks with plasticine and repeated the above procedure. The difference between the volume with plasticine and without plasticine provides a

Table 1 Bulk chemical analyses of all sampled bombs

Sample No.	GP17A	GP17B	GP8	GP9	GP10	GP11	GP6	GP3	GP14	GP13	GP15	GP12	GP16	GP5
(wt%)														
SiO_2	65.79	64.80	64.34	64.32	64.30	64.26	64.11	64.30	64.46	63.91	63.71	64.28	63.27	64.65
TiO_2	0.355	0.383	0.388	0.392	0.376	0.385	0.389	0.389	0.386	0.391	0.380	0.372	0.404	0.357
$Al2O_3$	16.39	16.56	16.77	16.72	16.82	16.83	16.78	16.67	16.67	16.95	17.21	16.98	17.05	16.97
FeO*	4.26	4.66	4.74	4.67	4.71	4.79	4.83	4.75	4.72	4.81	4.67	4.58	5.00	4.26
MnO	0.075	0.083	0.083	0.086	0.084	0.084	0.084	0.084	0.084	0.085	0.083	0.079	0.086	0.077
MgO	2.05	2.28	2.31	2.43	2.32	2.33	2.35	2.42	2.31	2.43	2.39	2.25	2.60	2.22
CaO	4.70	5.03	5.23	5.23	5.26	5.21	5.35	5.25	5.19	5.36	5.50	5.29	5.58	5.23
Na_2O	4.30	4.20	4.19	4.18	4.17	4.16	4.18	4.19	4.21	4.17	4.21	4.26	4.18	4.30
K_2O	1.96	1.89	1.82	1.84	1.82	1.82	1.79	1.84	1.85	1.77	1.73	1.78	1.70	1.81
P_2O5	0.120	0.127	0.129	0.131	0.126	0.125	0.130	0.128	0.130	0.129	0.126	0.123	0.128	0.124
(ppm)														
Ni	25	26	25	29	27	26	26	29	25	27	26	26	30	26
Cr	37	40	38	41	36	33	33	40	33	41	33	39	43	42
Sc	11	12	12	12	12	12	11	11	11	11	12	11	12	11
V	100	107	111	112	105	109	112	108	108	111	109	108	116	98
Ba	827	794	777	779	780	782	769	779	784	763	747	772	741	783
Rb	45	45	41	42	42	42	40	42	42	41	39	41	39	41
Sr	547	560	548	551	563	552	553	553	552	558	574	576	599	578
Zr	93	95	91	93	93	92	90	92	92	89	87	89	90	88
Y	9	10	10	10	10	8	10	10	10	9	10	9	11	9
Nb	2.6	3.0	2.6	2.6	3.9	2.3	3.0	2.7	3.6	2.7	3.2	2.8	2.2	2.6
Ga	15	20	18	17	17	17	16	16	18	17	18	17	19	19
Cu	46	48	45	48	60	67	57	55	50	52	93	52	47	44
Zn	65	69	64	69	63	67	65	65	66	68	63	63	68	62
Pb	9	10	6	11	8	7	9	8	9	10	8	9	9	8
La	10	9	12	13	14	14	12	10	13	10	11	11	12	7
Ce	21	29	23	27	28	22	19	27	25	28	26	25	27	30
Th	4	4	3	3	3	4	3	4	5	3	3	4	4	5

Analyses performed by the GeoAnalytical Laboratory at Washington State University (for analytical details see Johnson et al. 1999)
*Total Fe is expressed as FeO. All oxides normalized to 100% on a volatile-free basis

measure of crack volume with a reproducibility of approximately +/–2% (1σ).

We also measured average crack widths, depths, and orientations, and shapes of resulting polygonal crusts on individual bomb surfaces. Widths and depths were measured by hand on the samples themselves. Crack orientations were measured on digital images of bomb surfaces using the public domain program NIH Image. Individual crack orientations within single samples were combined in a rose diagram, with the dominant crack orientation normalized to 0° (north). The same images were used to determine both crack intersection angles and average lengths between crack intersections. The number of sides of constituent polygons formed by the cracks was counted manually on the same images. Bombs were then cut in half and the thickness of the glassy rind was measured perpendicular to the bomb surface. Rinds were distin-

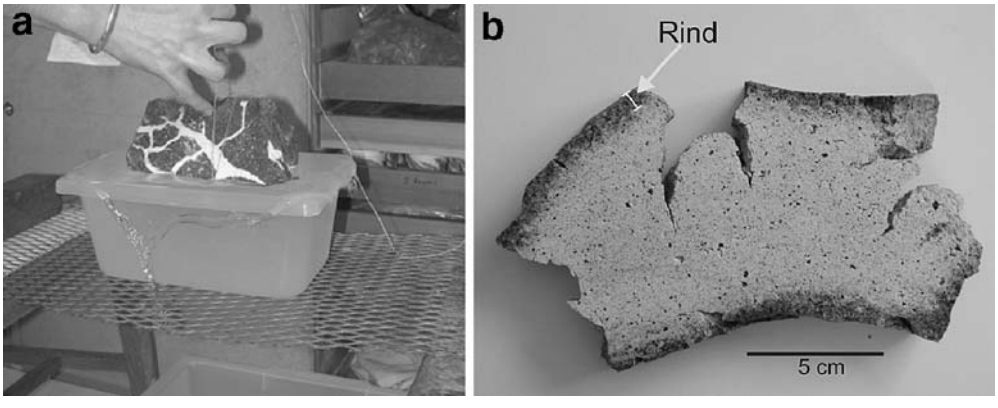

Fig. 4 **a** Measurement of breadcrust bomb (and crack) volume using Archimedes Principle. Cracks are filled with plasticine. **b** Polished slice through breacrust bomb GP8 (*TkB*) showing color and vesicularity changes from rind to interior. Cracks on the under surface are much less extended than those on the upper surface

guished on the basis of color and vesicularity differences (Fig. 4b).

Density, porosity, permeability, and vesiculation styles

To determine the bulk density (ρ_b) of bomb samples, we drilled one-inch diameter cores of bomb interiors, weighed the cores, and measured their volumes. Connected porosities (ϕ_c) were determined by comparing the He-accessible volume of the core with the bulk core volume, measured using a Micromeritics multi-volume He-pycnometer at the University of Oregon (e.g., Kuntz et al. 1981). At least 3 measurements were made per sample; resultant precision is +/–0.2% (1σ) of porosity value. Bulk porosities (ϕ_b) then follow as $\phi_b=1-(\rho_b/\rho_s)$, where ρ_s is solid density, which we approximate using the density of the most dense, non-vesicular bomb. The isolated porosity (ϕ_i) is defined as the difference between bulk and connected porosities, $\phi_i=\phi_b-\phi_c$. We determined the porosity of vesicular bomb rinds (ϕ_r) separately by extrapolation from two-dimensional backscattered electron (BSE) images of each sample, with precision of +/–5% (1σ).

Gas permeability of core samples was determined using a Porous Materials, Inc. capillary flow porometer at the University of Oregon. The porometer measures sample permeability by successively increasing the flow rate through a one-inch diameter core of sample material and measuring the differential pressure across the sample at each flow rate increment. A modified form of Darcy's Law, known as Forchheimer's equation (Innocentini and Pandolfelli 2001), accounts for the compressibility of air flowing through the sample and can be used to determine both Darcian permeability, k_1, and inertial permeability, k_2:

$$\frac{P_i^2 - P_o^2}{2PL_c} = \frac{\mu}{k_1}\nu_s + \frac{\rho}{k_2}\nu_s^2. \quad (1)$$

Here P_i and P_o are the pressure at the inlet and outlet of the sample respectively, L_c is the length of porous media along axis of flow (core length), μ is the viscosity of air, ρ is air density, ν_s is the superficial velocity (calculated by dividing the flow rate, Q, by the cross-sectional area, A), and P is the pressure of the fluid at which velocity and viscosity are measured. We use the Forchheimer equation with $P=P_o$ so that μ and ρ correspond to values at atmospheric pressure (e.g., Rust and Cashman 2004). At least two measurements were made per sample.

Qualitative characterizations and quantitative percentage determinations of vesicle and crystal populations were made using backscatter electron (BSE) images of polished thin sections of each sample. BSE images were obtained on a JEOL 6300 scanning electron microscope at the University of Oregon using a 10 keV electron beam at 10–20 nA sample current and a 15 mm working distance. Vesicularity is precise to +/–5% (1σ).

Fourier transform IR spectroscopy

Fragments of the glassy bomb rinds were selected for Fourier Transform infrared spectroscopic (FTIR) analysis to determine H_2O and CO_2 contents of matrix glass. At least two chips of each sample were doubly polished into wafers with two parallel sides. Samples were prepared to the maximum thickness that would allow analysis of glass in spots lacking phenocrysts (<0.35 mm). The thickness of wafers was measured using a micrometer, with precision of ±5 μm (1σ). While some workers have rejected FTIR for analysis of matrix glasses when glass areas are too small to analyze without hitting abundant small microlites (e.g., Harford et al. 2003), we take a different approach and intentionally use a wide aperture and large wafer thickness. Such an approach enables us to detect low CO_2 concentrations that are not detectable in more common measurements of small doubly intersected melt inclusions by other workers. We correct for microlites and bubbles by subtracting average microlite crystallinities and vesicularities from measurements of pathlength (e.g., Hammer et al. 1999). In addition, to check efficiency of degassing of bomb interiors, we prepared wafers of bomb interiors from a single sample of each breadcrusted bomb class.

Transmission spectra of the glassy bomb rinds were obtained using a Thermo Nicolet Nexus 670 FTIR spectrometer interfaced with a continuum IR microscope at the University of Oregon. We acquired a minimum of ten spectra on different spots on each wafer using a white light source and a square aperture length of 50–170 μm. Absorption band assignments for water and carbon dioxide species dissolved in rhyolitic glass were taken from Zhang et al. (1997) and Behrens and Tamic (2004), respectively. Absorptions (peak heights) were measured by subtracting background fits using straight line fits and were used to determine species concentration through Beer's Law, or modifications of this law (e.g., Zhang et al. 1997).

In the IR region, complexities within the band at 3,550 cm^{-1} attributed to molecular H_2O make use of individual species peaks at 5,230 and 4,520 cm^{-1} preferable for measurement of H_2O_{mol} and OH^- (Zhang et al. 1997). Total water concentration was calculated using these near-IR absorption peaks according to the calibration technique of Zhang et al. (1997). This method alleviates the need for determining molar absorption coefficients for each band, an inherently difficult calculation due to the dependence of each on total water content. The resultant expression is a modified form of Beer's Law and represents an empirical fit to available data. The technique is calibrated for dissolved water in rhyolitic glasses and is expected to be accurate for $H_2O_{total} \leq 5.5$ wt% (Zhang et al. 1997). We assume that the samples have not been hydrated, as timescales for H_2O diffusion into the glassy rinds that would significantly affect measurement over >50 μm length (minimum aperture dimension used) are long compared to the 3 years between eruption and sample collection (Friedman et al. 1966).

The band at 2,350 cm^{-1} is attributed to molecular CO_2 (Newman et al. 1988) and can be used to determine the relative concentration of CO_2 (c) directly as $c=(MW\ Ab)/\varepsilon d_s \rho_{gl}$, where MW is the molecular weight of CO_2, Ab is the absorbance of the sample at specified wavelength, ε is the molar absorption coefficient, d_s is the thickness of the glass sample (pathlength), and ρ_{gl} is the room temperature density of the glass. We use ε=1,214 L/mol-cm based on measurements of synthesized rhyolitic samples (Behrens and Tamic 2004). Sample thickness (d) was corrected for microlite content and vesicle percentage using microlite crystallinities and porosities, respectively, determined through two-dimensional image analysis of each bomb. We extrapolate crystallinity measurements of two-dimensional images to three dimensions, by assuming that microlite crystallinity is similar in all directions (+/–2% crystallinity). We checked this approximation for flow banded sample GP3, which contains aligned microlites and found that measured crystallinity varies by less than +/–2% in perpendicular directions. This corresponds to variation in calculated H_2O and CO_2 content that is less than precision calculated for variation between wafers of the same sample. In addition, the presence of phenocrysts in analysis spots decreases the effective pathlength of wafers. Because we cannot determine the percentage of the beam window occupied by phenocrysts, we report the average of maximum H_2O and CO_2 concentrations calculated for each wafer; error bars (1σ) quantify variation between wafers of the same sample. Glass densities (ρ_{gl}) were calculated using the method compiled by Spera (2000), based on matrix glass compositions of each sample (from electron microprobe analysis) and iteration of the water concentration.

Results

The analyzed blocks and bombs are divided into four morphologic categories (Fig. 3). We use the details of these morphologic categories as a framework for examining physical characteristics of our samples. Dense blocks (DB) lack both glassy quench rinds and a breadcrusted surface (GP17a, GP17b; Fig. 3a). Thickly breadcrusted bombs (TkB) have dark glassy rinds and widely spaced, deep cracks (GP8, GP9, GP10, GP11, GP6; Fig. 3b). Foliated, intermediate breadcrust bombs (FIB) have poorly defined rinds of intermediate thickness and density, more closely spaced cracks than TkB, and pervasive flow-banding that is not parallel to bomb faces (GP3, GP14; Fig. 3c). Thinly breadcrusted bombs (TnB) are the most highly expanded and are characterized by closely spaced cracks that intersect in polygonal patterns (GP13, GP15, GP12, GP16, GP5; Fig. 3d–f). All bombs are characterized by prismatic bomb morphologies, although the shapes of vesicular bombs are slightly more curved (convex outward). Cracks are equally distributed across bomb faces, with the exception of TkB bomb GP8. This bomb has wider, deeper cracks on the upper surface than on the lower surface.

Two bombs have unusual breadcrusting styles. These bombs display two distinct sets of breadcrust surfaces, one with a thicker, glassier rind, and the other with a thinner, more vesicular rind (Fig. 5). Each of these bombs (TkB bombs GP11 and GP6) is inferred to be a piece of an original bomb that split into two separate pieces upon impact with the crater floor, exposing a secondary surface to the air after breakage. We suggest that the thick, glassy surface (Fig. 5, surface A) was exposed upon fragmentation (primary breadcrust surface); whereas the thin, vesicular surface was exposed upon impact (Fig. 5, surface B, secondary breadcrust surface). Breakage of bombs upon impact is supported by the presence of corresponding secondary breadcrust surfaces on the bombs sitting adjacent to GP6 and GP11 on the crater floor, presumably the other halves to originally larger bombs. We assume that vesiculation was virtually complete by the time of impact, as vesicular, secondary breadcrust surfaces have approximately the same bulk porosity as bomb interiors.

Surface cracks

Patterns of surface cracks vary with rind thickness and vesicularity. TkB clasts have average crack depths >1 cm and cracks intersect at angles of <100° (Fig. 6a; Table 2). Cracks are widely spaced, averaging >2.5 cm between intersections, form sets that are roughly orthogonal, especially on the more prismatic bomb faces, and create polygons with an average of 3.8–4.8 sides (Fig. 3b). FIB have intermediate crack depths. The average spacing between crack intersections is large in comparison with spacing for other bomb types (3.7 and 4.7 cm), with variable angles between intersecting cracks creating

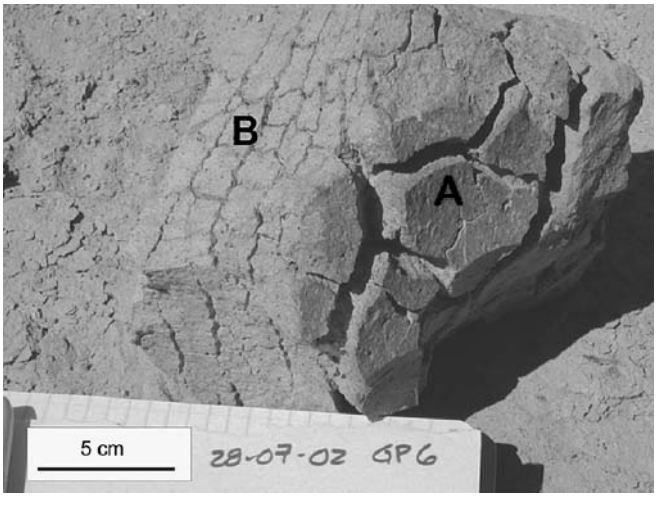

Fig. 5 GP-6 (TkB) displays two distinct breadcrust surfaces. One quenched and cracked surface formed prior to impact (surface *A*). The newly exposed face (surface *B*) then quenched and cracked due to further inner expansion, forming a new breadcrust pattern with a thinner bomb rind than surface A

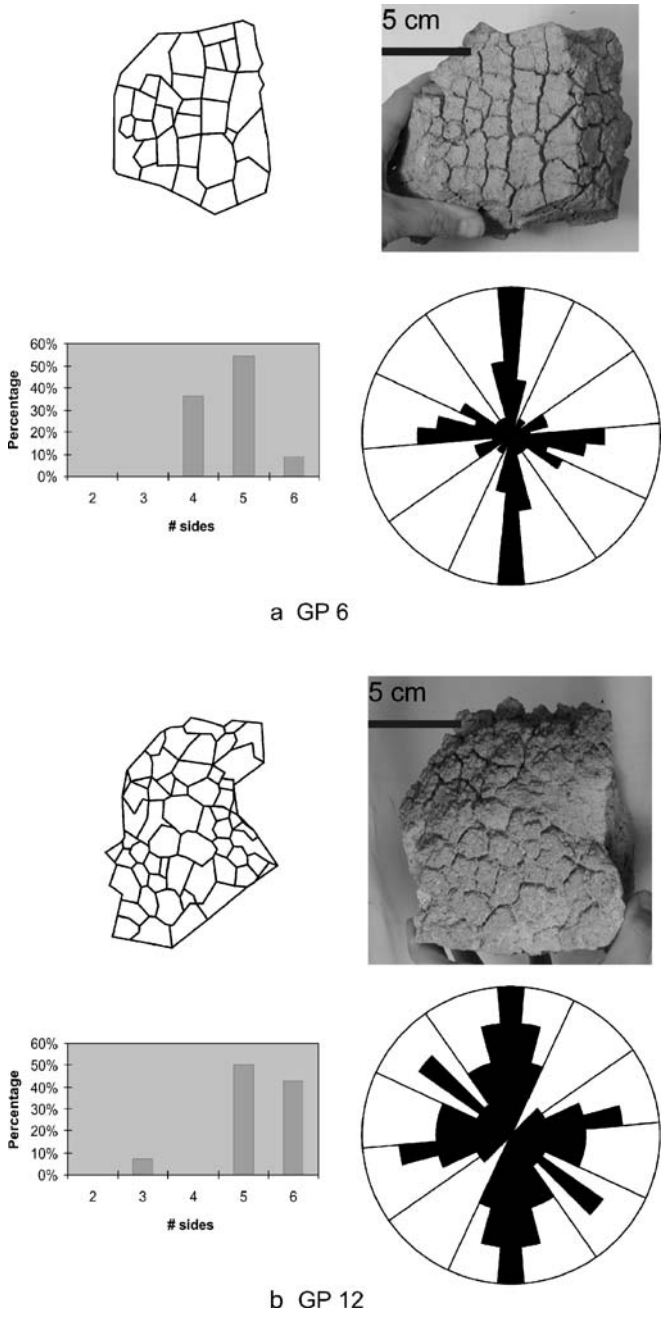

Fig. 6 Photographs of surface crack patterns and rose diagrams of crack orientations, with the highest orientation percentages normalized to extend to diagram maximum. Rose diagram bin size is 10°; measurement units are number of cracks. **a** Crack orientations of GP6 are typical of TkB, with approximately perpendicular cracks and an average of 4–5 polygon sides **b** Crack orientations of GP12 are typical of TnB, with cracks intersecting at >100 degrees, in crack patterns formed by 5–6 sided polygons

polygonal patterns. TnB have shallow cracks that intersect at angles >100° (Fig. 6b). Cracks on these bombs are closely spaced, averaging <2.5 cm between crack intersections, and form pentagonal to hexagonal patterns.

Bomb rinds

The thickness of quenched rinds correlates with the type of crack pattern. DB and FIB bombs lack distinct glassy rinds and have either no (DB) or poorly organized (FIB) crack patterns. In contrast, bombs with well developed crack patterns have well-defined glassy rinds with thicknesses >3 mm (TkB) or <3 mm (TnB). The porosity of these glassy rinds varies from ~0% in TkB clasts to 30–54% in TnB clasts (Table 2).

We assume that bomb rinds quench rapidly and therefore preserve textures and volatile contents of the magma prior to fragmentation. Each morphologic class preserves a limited range of H_2O and CO_2 in the matrix glass; there are pronounced differences in glass volatile content between different morphologic types. DB bomb exteriors have low water contents (0.3–0.4 wt%) but measurable CO_2 (6–9 ppm). TkB rinds have H_2O contents of 1.0–1.3 wt% and also preserve measurable CO_2 (7–17 ppm). In contrast, FIB outer surfaces have intermediate H_2O contents (0.5–0.9 wt%) but no CO_2. TnB rinds also have no measurable CO_2 despite preserving high water contents (1.4–3.1 wt%). Given the assumption that measured water and CO_2 values represent the volatile contents of the melt at fragmentation and the knowledge that the solubility of volatile species is dependent upon pressure, these data indicate that magma was tapped from a range of conduit levels during each individual Vulcanian event. The data also suggest thatthe magma that fragmented to form different bomb types experienced different degassing histories.

Rind water contents decrease with increasing rind thickness (Fig. 7) and samples with rind H_2O contents <~0.9 wt% lack vesicularity gradients that distinguish breadcrust rinds (DB and FIB bomb types). This minimum water value for breadcrust rinds is slightly higher than the threshold value of 0.4 wt% determined by Hoblitt and Harmon (1993) for syn-eruptive vesiculation of cryptodome dacite at Mount St. Helens. The highest measured value for DB bombs alone, however, is 0.4 wt% H_2O. Magma with pre-fragmentation H_2O contents between 1.0 and 1.3 wt% produced TkB bombs, while magma containing >1.4 wt% H_2O produced TnB bombs on eruption. The observed relationship between rind thickness and H_2O content suggests that breadcrust bomb textures are dictated by variations in pre-fragmentation H_2O content.

The transition from relatively dense rinds to more vesicular clast interiors in TkB and TnB bombs is characterized by a diffuse zone of vesiculation that is heterogeneous in directions both parallel and perpendicular to the bomb surface (Fig. 8a). Vesicles in this transition zone occur in clusters and are commonly elliptical in cross section (Fig. 8b). Individual clusters are not concentrated around particular crystal phases, but instead form discontinuous bands that show no particular orientation to either phenocryst surfaces or bomb faces (Fig. 8c). By analogy with FIB clasts, it seems likely that these diffuse vesicular bands may reflect cryptic flow banding within the magma.

Table 2 Crack properties, porosity, and permeability of all sampled bombs

	Sample#	Rind thickness (mm)	Average crack depth (cm)	Average angle between cracks (°)	Average length between crack intersections (cm)	Average number of polygon sides	V_v=interior vesicle volume formed post-fragmentation (cm^3)	V_p=predicted crack volume (cm^3)	V_m=measured crack volume (cm^3)	Rind porosity, Φ_r (%)	Bulk interior porosity, Φb (%)	Connected interior porosity, Φ_c (%)	Isolated porosity Φ_I(%)	Darcian permeability (m^2)	Inertial permeability (m)	H_2O in rind matrix glass[f] (wt%)	CO_2 in rind matrix glass[f] (ppm)	H_2O in interior matrix glass[f] (wt%)
(DB)	GP-17a	_	[a]	[a]	[a]	[a]	0	0	0	0	1	1	0	2.3E-17	[e]	0.3	6	[e]
	GP-17b	_	[a]	[a]	[a]	[a]	0	0	0	22	30	29	1	7.8E-13	[e]	0.4	9	[e]
(TkB)	GP-8	7.2	3.3	99	5.4	3.8	896	213	460	0	56	44	12	2.2E-14	2.2E-12	1.3	9	0.2
	GP-9	6	2.2	82	3.2	4.3	138	48	67	0	47	35	11	5.4E-15	2.5E-11	1	8	[e]
	GP-10	5.4	1.3	92	3.4	4.2	270	72	106	1	57	46	12	4.4E-14	2.0E-12	1	17	[e]
	GP-11	4.8	1.0 and 0.4[b]	96	4.7	c and 4.8[b]	[c]	[c]	[c]	2 and 59[b]	[d]	[d]	[d]	[d]	[d]	1.3	14	[e]
	GP-6	3.4	1.3 and 0.5[b]	99	2.6	3.8 and 4.7[b]	[b]	[b]	[b]	13 and 65[b]	64	57	7	2.9E-14	3.7E-11	1.2	10	[e]
(FlB)	GP-3	_	0.9	97	3.7	c	[c]	[c]	[c]	12	40	35	5	2.2E-14	1.2E-11	0.9	0	[e]
	GP-14	_	0.6	115	4.7	c	[c]	[c]	[c]	10	32	30	2	3.0E-14	6.7E-12	0.5	0	0.4
(TnB)	GP-13	2.8	0.7	108	2.4	5.3	[c]	[c]	[c]	46	55	47	8	4.9E-14	1.9E-11	2.1	0	[e]
	GP-15	2.1	0.8	109	2.1	5.3	[c]	[c]	[c]	30	71	63	8	4.5E-12	1.2E-09	1.4	0	0.2
	GP-12	1	0.5	104	1.8	5	[c]	[c]	[c]	41	62	53	9	9.9E-14	7.7E-11	2	0	[e]
	GP-16	0.4	0.7	112	1	5.4	[c]	[c]	[c]	40	71	63	8	5.9E-14	4.0E-11	1.8	0	[e]
	GP-5	0.4	0.4	106	1.5	5.8	39	1	15	54	71	62	9	1.5E-12	6.3E-09	3.1	0	[e]

[a]These bombs do not have surface cracks
[b]These bombs contain two distinct sets of breadcrust surfaces
[c]These samples were partial bomb samples
[d]This bomb was too small to drill a one-inch core
[e]Not analyzed
[f]From FTIR spectroscopy; using 5,230 and 4,520 cm^{-1} peaks for rind H_2O content, but 3,550 cm^{-1} peak for interior H_2O content due to low water concentration of interior glass, using Beer's Law with ε=80 L/mol-cm

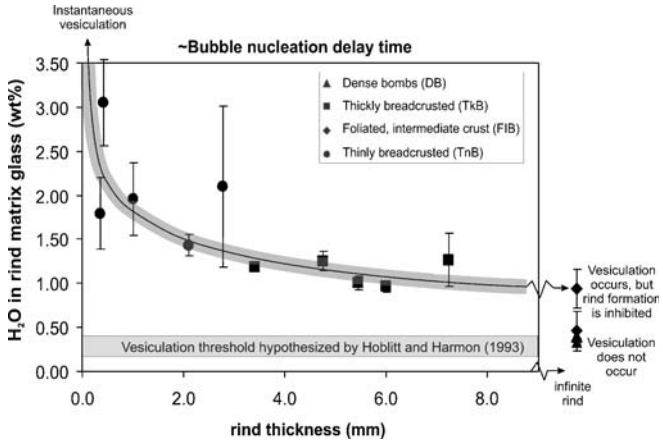

Fig. 7 Ballistic bomb rind water content versus rind thickness. 'Infinite rind' refers to samples that do not contain a discrete transition from dense rind to vesicular interior

Bomb interiors

A distinctive characteristic of breadcrusted bombs is the contrast in vesicularity between denser glassy rinds and vesicular interiors. The porosity of bomb interiors ranges from 0 to 71% (Table 2). DB samples range in bulk vesicularity from near 0 to 29%, with no apparent vesicularity variations from core to rim. FIB bombs have moderate bulk vesicularities (32–40%) and although they lack well-defined, discrete glassy rinds, vesicularity is somewhat higher in the interiors than close to crudely breadcrusted surfaces. TkB bombs have interior vesicularities of 47–64%, with a transition outwards to dense (0–13%) glassy rinds. TnB samples have the highest bulk vesicularities (55–71%), transitioning outwards to rinds of slightly lower vesicularities (30–54%). Matrix glass volatile contents of interiors are lower than in corresponding rinds, in agreement with vesicularity variation between bomb interiors and rinds. All breadcrusted bombs lack CO_2 in vesicular interior matrix glass; however, TkB bomb GP8 and TnB bomb GP15 contain 0.2 wt% H_2O, and FIB bomb GP14 contains 0.4 wt% H_2O.

Bomb expansion probably ceased when bubble networks within the bomb became sufficiently connected to permit permeable flow of gases out of the bomb interior. Above this critical permeability, interior expansion and resultant exterior expansion-related cracking would cease, although interior gas exsolution may continue. We determined the connectivity of interior bubble networks in two ways. Comparison of bulk (ϕ_b) and connected (ϕ_c) porosities of individual samples provides a measure of the isolated porosity (ϕ_i; Table 2). We also measured permeability directly. Sampled bombs show connected porosities of $1 \leq \phi_c \leq 63\%$, isolated porosities of $0 \leq \phi_i \leq 12\%$, and permeabilities of $2.3*10^{-17} \leq k_1 \leq 4.5*10^{-12}$ m^2. Not surprisingly, DB bombs, with low bulk porosities, have the lowest connected porosities. TnB bombs, with the highest bulk porosities, also have the highest connected porosities, while TkB bombs have the highest isolated porosities. The permeability of the vesicular interior of both TnB and TkB clast types is similar and lower than many other vesicular samples with similar values of connected porosity (e.g., Klug and Cashman 1996; Rust and Cashman 2004). Exceptions to low permeability values include FIB bombs with sub-aligned vesicular flow-bands, moderately vesicular sample DB GP17b, and TnB sample GP16.

Discussion

The data presented above allow us to address several different questions related to the origin of Vulcanian eruptions. We start by examining the processes involved in breadcrust bomb formation, including the times available after fragmentation for glassy rind formation and pre-impact expansion and the relationship between breadcrust styles and different breadcrusting mechanisms. We then relate post-fragmentation expansion to differences in pre-fragmentation volatile contents and the resulting response to syn-eruptive decompression and cooling. The preserved volatile contents of glassy breadcrust rinds permit us to estimate the pressure of pre-fragmentation storage, thus constraining conditions that led to pressurization (and eventual eruption) of the shallow conduit. Finally, we combine these observations with seismic data to develop a general model of Vulcanian eruptions at Guagua Pichincha in 1999.

Timing of breadcrusting

The absence of bubbles in breadcrust bomb rinds compared to vesicular interiors suggests that the primary control on the formation of glassy rinds is a bubble nucleation delay. We suggest that the delay time for bubble nucleation is inversely proportional to initial volatile content, such that the glassy rind thickness increases with decreasing H_2O content (Fig. 7, e.g., Hoblitt and Harmon 1993). To test this hypothesis, we use GP6, which has both a glassy pre-impact and a vesicular post-impact breadcrust surface (Fig. 5), to place constraints on the time scales of vesiculation and rind formation. Flight trajectories for a 20-cm diameter bomb with a final landing position approximately 800 m from the vent (Eject! 1.1; Table 3; Mastin 2001) require an ejection velocity of ~100 m/s for ejection angles between 30 and 60 degrees and limit the time between ejection and impact to 10–17 s (Fig. 9). The maximum nucleation delay time for this sample must have been <<10–17 s (assuming negligible time between fragmentation and ejection from the vent), to allow complete vesiculation and expansion prior to impact.

An independent measure of nucleation delay time is provided by the thickness of the glassy rind if we assume that vesiculation cannot occur below the temperature of the glass transition T_g. We estimate T_g using Sowerby and Keppler's (1999) calorimetric determination for low-water content rhyolite glass. Cooling during flight is achieved by both radiation from the bomb surface and advective cooling provided by the movement of the bomb through

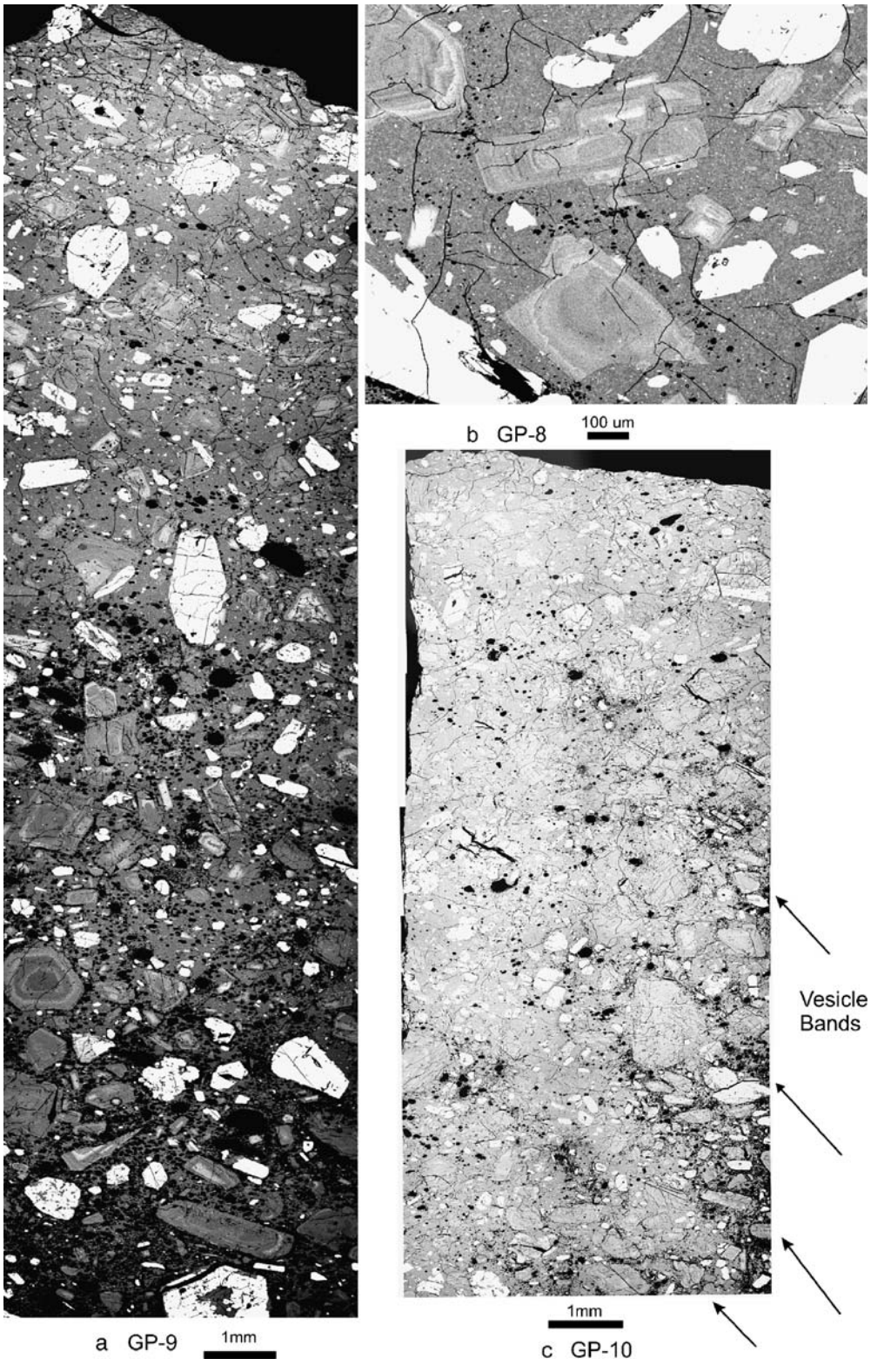

Fig. 8 SEM backscatter electron images of three TkB bombs. **a** vesiculation from rind (image *top*) inward in GP-9, **b** *arrows* denote vesicle bands in GP-10, and **c** fine scale heterogeneous bubble nucleation in GP-8

the air, in addition to conductive cooling within the bomb interior (Thomas and Sparks 1992). Following Thomas and Sparks (1992), we calculate the cooling time for GP6 based on the 3.4 mm rind thickness. Heat is lost from the bomb surface via both forced convection (F_c) and radiation (F_r):

$$F_c = h_c(T_s - T_\infty) \tag{1a}$$

Table 3 Input parameters to Eject! simulation

Input parameters to Eject! simulation:	
Bomb density:	2,500 kg/m^3
Bomb diameter:	20 cm
Elevation of crater:	4,784 m
Variable cd (drag coefficient) for bomb shape:	Sphere
Tailwind speed:	0 m/s
Temperature at sea level:	25°C
Thermal lapse rate:	6.5 C/km
Extent of zone of reduced drag:	0 m

$$F_r = \gamma\left(T_s^4 - T_\infty^4\right) \tag{1b}$$

where h_c is the convective heat transfer coefficient, γ is the black body emissivity, T_s is the surface temperature, and T_∞ is the ambient temperature. Convective heat loss depends upon the heat transfer coefficient, h_c, which is a function of the flow conditions as characterized by the Reynolds number (Re):

$$Re = \frac{ud\rho}{\mu}, \tag{2}$$

where u is the average velocity, d is the particle diameter, ρ is the air density at elevation, and μ is the air viscosity. We approximate flight conditions by assuming a spherical bomb shape of 10 cm radius, 4,784 m altitude of crater, 77 m/s average velocity of particle (from the ballistics model), and atmospheric density and air viscosity relations used by Thomas and Sparks (1992; Table 4). The heat transfer coefficient for this sphere is then calculated using

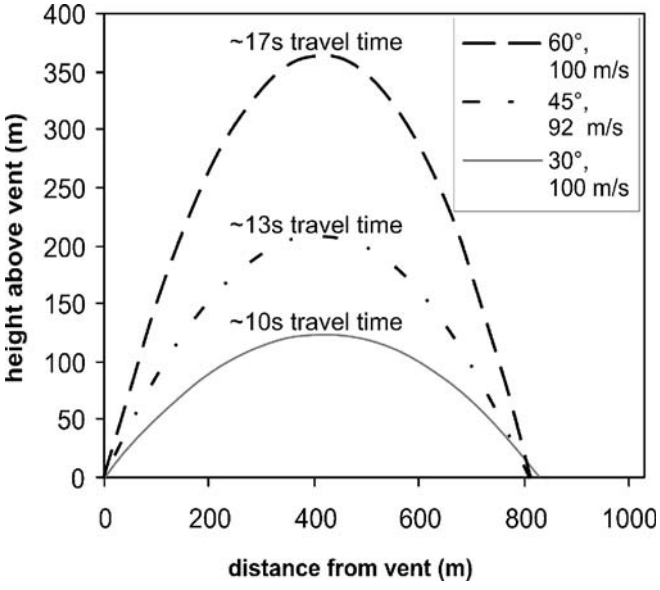

Fig. 9 Flight times of GP-6 (TkB) calculated using Eject!, (Mastin 2001). 60 and 30° profiles were calculated for 100 m/s initial velocity; 45° profile was calculated for 92 m/s initial velocity

the empirical relation of Achenbach (Thomas and Sparks 1992) for $3\times10^5<Re<5\times10^6$ as

$$\frac{h_c d}{k_a} = 430 + aRe + bRe^2 + cRe^3, \tag{3}$$

where k_a is the conductivity of air, and the constants are $a=5\times10^{-3}$; $b=0.25\times10^{-19}$; $c=-3.1\times10^{-17}$.

Conductive cooling within the bomb is approximated using the one-dimensional relation for an isotropic sphere with no heat production and uniform thermal characteristics:

$$\frac{\partial^2 T}{\partial r^2} + \frac{2}{r}\frac{\partial T}{\partial r} = -\frac{1}{\kappa}\frac{\partial T}{\partial t}, \tag{4}$$

where T is temperature, r is the radial distance from the clast center, κ is the thermal diffusivity of the particle, and t is the time. This equation was solved for a 10-cm-radius clast assuming an air temperature of 0°C, initial bomb temperature of 880°C and a heat flux from the surface of

$$F_t = h_c(T_s - T_\infty) + \gamma(T_s^4 - T_\infty^4). \tag{5}$$

Temperature–time profiles calculated for different radial distances within the clast indicate that quenching of the 3.4 mm outer bomb rind of GP-6 would require ~11 s. Therefore, the bomb must have traveled through the air for ~11 s prior to impact to have (1) formed a glassy rind and (2) vesiculated prior to the impact that generated the second crack face. This time scale is consistent with calculated ballistic flight times of <17 s if vesiculation, once initiated, was rapid.

The same cooling model can be used to determine the range of cooling times required to produce the range of rind thicknesses observed in all TkB and TnB bombs (0.4–7.2 mm; Fig. 10). We note that calculated quenching times are maxima, as they were calculated for the maximum bomb radius (10 cm) and we assumed negligible vesicularity. Maximum estimated cooling times range from <1 to 45 s from the thinnest to thickest bomb rinds.

Table 4 Input parameters to cooling calculation

Input parameters to cooling calculation:	
Bomb density:	2,500 kg/m^3
Bomb radius:	10 cm
Elevation of crater:	4,784 m
Ambient temperature (T_∞):	0°C
Initial bomb temperature:	880°C
Heat transfer coefficient (h_c):	453 W/m^{2}K
Thermal conductivity of air (k_a)*:	0.024 W/m·K
Air density at elevation (ρ):	0.721 kg/m^3
Air viscosity (μ)[a]:	$1.71\cdot10^{-5}$ kg/m·s
Average velocity of bomb (u):	77 m/s
Thermal diffusivity of particle (κ)*:	$3.0\cdot10^{-7}$ m^2/s
Black body emissivity (γ)*:	$5.669\cdot10^{-8}$ W/m^2·K^4

[a]From Thomas and Sparks (1992)

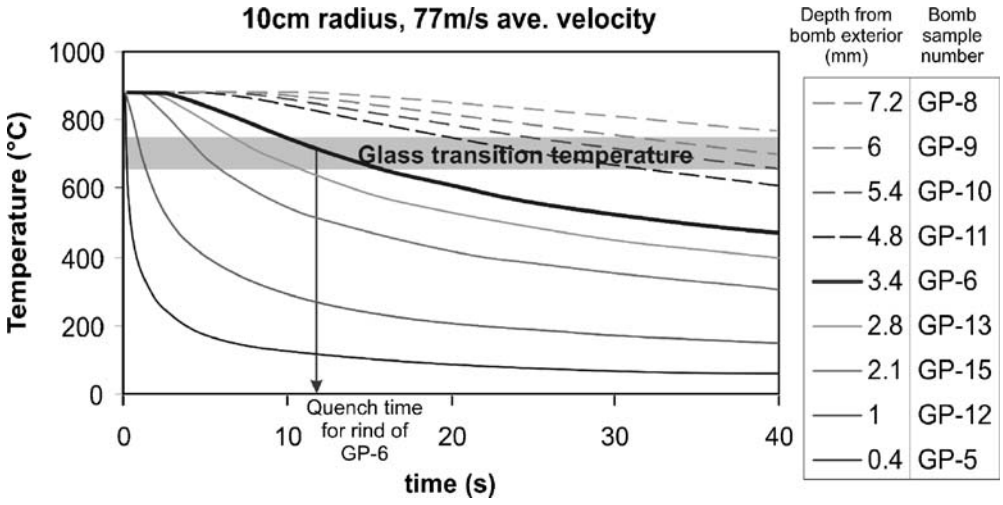

Fig. 10 Cooling paths for varying depths beneath rind surface calculated for a 10 cm radius bomb at 77 m/s average velocity with Tg estimates from Sowerby and Keppler (1999). *Arrow* points to approximate cooling time for rind of bomb GP-6; see discussion in text. An initial bomb temperature of 950 and 800°C increases and decreases this cooling time by 3.5 s respectively

A simple comparison of calculated cooling times with the flight time estimates for GP6 shows that thin (TnB) bomb rinds quenched and interior vesiculation was complete well before the clasts reached the crater floor, while vesiculation in the bombs with longer cooling times (TkB) appears to have continued well after ejection and impact. This difference may be responsible for increased rounding of TnB clasts over TkB clasts. In contrast, a calculated rind quench time of ~45 s would have allowed ample time for post-impact vesiculation. This interpretation is supported by the morphology of GP8 (TkB), which has a bulged upper surface that is more expanded than the lower surface (Fig. 4).

Nature of breadcrusting

Cracks may form in bomb surfaces by three different mechanisms: interior expansion after outer rind formation, thermal contraction of the rind, and stresses applied during impact. All three mechanisms probably contribute, in various proportions, to the surface morphology of breadcrust bombs. In the field we distinguished impact-generated fractures by their radial character; rare bombs with this cracking signature were not collected for this study. Therefore, we consider only thermal and expansion driven fracture.

Inferred post-fragmentation expansion ($\Delta\phi=\phi_b-\phi_r$) varies from 0 in DB clast GP17a to a maximum of 51% in TkB clast GP6. FIB clasts, which lack well defined rinds, and TnB clasts, with variably vesicular rinds, have $\Delta\phi$ values that lie between these two extremes. If the outer surfaces of the bombs quenched prior to vesiculation, the breadcrust cracks should accommodate all syn-eruptive interior expansion. For thin bomb rinds and moderate degrees of expansion, expanded interior vesicle volumes should exceed crack volumes (assuming spherical bomb shapes and triangular cross-sectional crack geometry; Fig. 11; Appendix). To test this hypothesis, we compare the expansion-related predicted (V_p) and measured (V_m) crack volumes for all complete bombs (Fig. 12). Predictions of crack volume based on expansion alone assume that the cracks propagate only as deep as the less vesicular, glassy rinds. V_p is given by

$$\frac{4}{3}\pi\left(\left(\left(r_i^3\left(\frac{1}{1-\Delta\phi}\right)\right)^{\frac{1}{3}}+t\right)^3-r_i^3\left(\frac{1}{1-\Delta\phi}\right)-(r_i+t)^3+r_i^3\right),$$

where r_i = radius of interior (pre-expansion), and t = thickness of rind. To calculate pre-expansion radii of bomb interiors, we use measurements of bomb volume, rind thickness, and average crack depth and assume spherical bomb shapes and triangular cross-sectional crack geometry. We find that V_m is much larger than V_p for TnB bombs (15 times greater) and somewhat larger than V_p for TkB bombs (1–3 times greater; Table 2; Fig. 12).

The clear evidence for internal expansion provided by the pronounced difference in bomb rind and interior vesicularities indicates that crack formation in many samples must occur primarily in response to post-fragmentation vesiculation. However, we suggest several additional deformation mechanisms to account for the discrepancy in crack volumes and the morphology of the breadcrust bombs. Firstly, we find evidence for ductile bending of bomb surfaces (Fig. 11b). Such bending increases measured crack volumes and produces concave surface profiles of some bomb faces, where the edges of surface polygons have inflated from pre-expansion radial positions. We also find evidence for thermal contraction-related cracking of bombs. The thermal origin of some cracks is supported by the observation that glassy rind thicknesses are typically less than corresponding crack depths (Table 2), indicating that vesiculation and vesiculation-driven expansion ceased prior to the final extent of crack propagation (Fig. 11a,c). If these cracks were created by expansion, then there should be a difference in vesicularity above and below crack tips; we do not see such a difference. Furthermore, thermal contraction creates cracks in the latest stage of bomb formation, producing cracks on the impact-generated surface of GP6, where the surface vesicularity is approximately the same as that of the interior (Table 2). Finally, we do not see evidence for decoupling between deformation behavior of the bomb rinds and interiors (Fig. 11d).

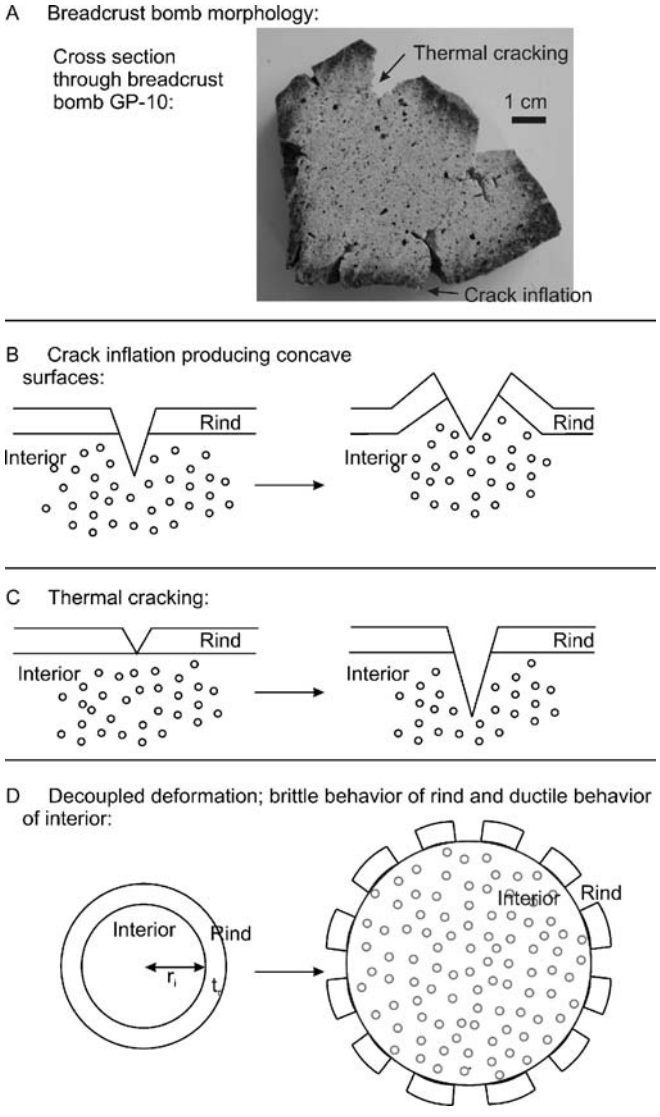

Fig. 11 **a** Cross-section through breadcrust bomb GP-10 (TkB), displaying inferred evidence of both: **b** crack inflation and **c** thermal cracking, as opposed to **d** decoupled behavior of rind and interior; brittle deformation of the rind around an expanded, vesicular interior. The rind is defined as the dense (lower vesicularity) outer portion of the bomb, distinguished on the basis of color and vesicularity differences. Both crack inflation and thermal cracking may continue after expansion-related cracking ceases

We can combine observations of crack geometry with cooling-time constraints provided in the previous section to construct the post-fragmentation history of TnB and TkB breadcrusting styles. The shallow depth of the cracks and short cooling times calculated for TnB bomb types, together with the low values of post-fragmentation expansion ($\Delta\phi$), suggest that the contribution of expansion to crack formation may have been small, in which case the cracks would record primarily thermal contraction of the thin glassy rind. In contrast, the deep cracks, relatively long quench times and the large values of $\Delta\phi$ of TkB bombs point to expansion as the predominant driving force behind crack formation. Expansion is also evident from the concavity of individual polygonal bomb surfaces, the convexity of crack surfaces, and the convex upper surface of GP8, the most obvious indication of protracted post-impact vesiculation.

The shape of polygons formed by intersecting cracks also provides clues about crack formation. Polygon formation has been studied for corn starch-water mixtures, where cracking does not reflect expansion, and contraction results from dessication rather than cooling. Here, the number of polygon sides is controlled by the shrinkage rate, with higher rates of contraction preferentially forming pentagons and lower rates preferentially forming hexagons (Toramaru and Matsumoto 2004). These studies may be most pertinent to TnB bombs, where polygons range from 5 to 6 sided and rind thickness correlates with the average number of polygon sides (Table 2), perhaps reflecting differences in expansion rates. In contrast, TkB bombs have mostly rectangular faces, a geometry that does not appear to be consistent with uniform volumetric expansion. Instead, crack formation appears to have been strongly influenced by the original prismatic morphology of the bombs. Support for this interpretation is provided by the orientation of rectangular fractures subparallel to the bomb sides. Cross sections of these bombs show that the edges have thicker glassy rinds than flat bomb faces (Fig. 4, bottom right corner), indicating faster post-fragmentation cooling along edges as a result of heat radiation in many directions. We suggest that by the time bomb expansion began cracks were more easily opened parallel to these thick (more rigid) edges. Subsequent cracks then propagated perpendicular to the direction of maximum principal stress, which is parallel to existing cracks (Müller 1998), such that cracks meet orthogonally. Faster cooling of bomb edges also explains the preservation of prismatic morphologies during expansion.

Limits to post-fragmentation expansion

If bomb expansion were limited only by the original dissolved volatile content, then most of the clasts should expand to very high vesicularities (Thomas et al. 1994). We would expect vesiculation >97% for TkB and TnB bombs (using an ideal gas approximation for difference in water content between rinds and interiors in GP8 and GP15). However, volumetric expansion will occur only as long as the rate of gas exsolution exceeds the rate of gas escape from the sample by permeable flow. Most samples have permeabilities that are low relative to those of other vesicular pyroclasts and dome lavas with a similar connected porosity range (Fig. 13; Table 2). Interior vesicularities of breadcrusted (inflated) clasts range from 32% (30% connected porosity) in an FIB bomb, to 71% (63% connected porosity) in the most vesicular TnB bomb. We interpret the low interior vesicularities, high interconnectivity, and high permeability of FIB clasts to reflect efficient bubble coalescence and gas escape along vesicular flow bands.

It seems likely that the low permeabilities of breadcrust bomb interiors reflect highly contorted gas pathways

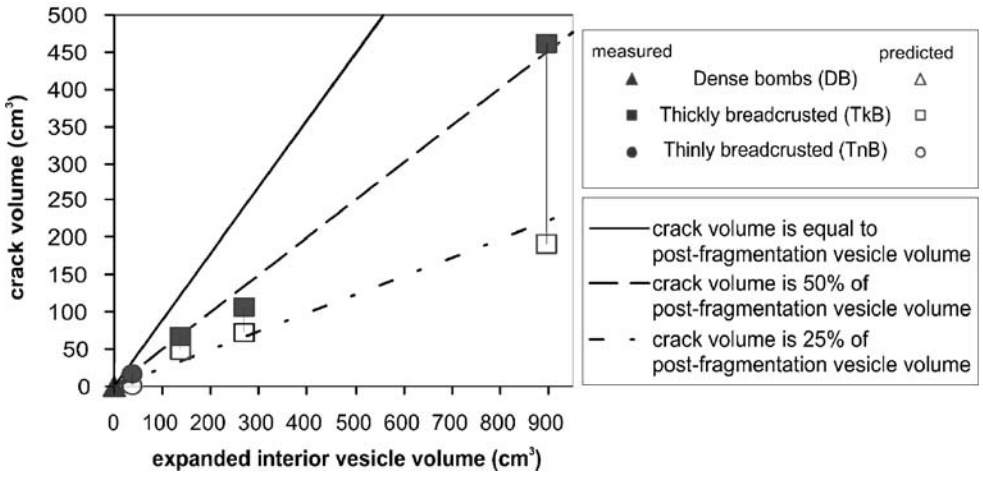

Fig. 12 Predicted vs. measured crack volume/bomb interior volume (v_c/v_i). Note that all crack volumes are larger than predicted given interior expansion volumes

caused by the percentage of isolated pores in TkB and TnB samples. Isolated porosities >5–10% are rarely identified in pumice from Plinian fall deposits (Klug and Cashman 1996; Klug et al. 2002), dome lavas (Formenti et al. 2003) or silicic lava domes (Rust and Cashman 2004) but are more common in pumice samples from pyroclastic flows (Klug et al. 2002). The presence of isolated pores reflects limited bubble coalescence. The film thinning required for coalescence development is most likely driven by bubble expansion (e.g., Klug and Cashman 1996). From this perspective, limited bubble coalescence might be expected under conditions where the time available for the process is short (e.g., rapid decompression following caldera collapse; Klug et al. 2002), melt viscosities are high, and/or overpressures driving expansion are small (as is expected for vesiculation of partially degassed melt, forming breadcrust bombs).

To summarize, the permeability data suggest that enhanced permeability in flow-banded samples is a result of high vesicle connectivity along bands. Post-fragmentation vesiculation resulted in a bubble population with limited connectivity, while still being permeable enough to allow gas escape from bomb interiors such that bomb vesicularities do not reach 97%. The low overall permeabilities and high percentage of isolated pores in TkB and TnB bomb interiors suggests that bubble coalescence was slow relative to bubble growth, perhaps a characteristic of slow expansion at small overpressures.

Pre-eruptive storage conditions

In Vulcanian eruptions, a fragmentation wave has been shown to propagate downward through the conduit at ~tens

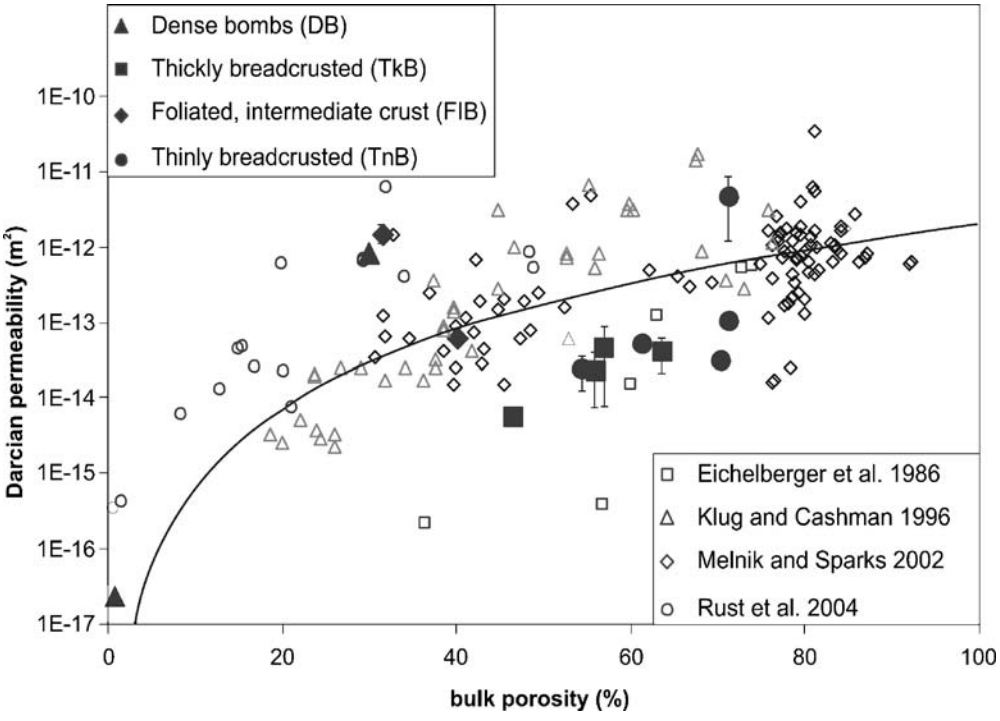

Fig. 13 Permeability–porosity relationship. Breadcrust bomb data in *large filled symbols* (note relative lower permeability of bombs in this study), *smaller unfilled symbols* represent data from: Eichelberger et al. 1986 (*squares*); Klug and Cashman 1996 (*diamonds*); Melnik and Sparks 2002 (*circles*); and Rust and Cashman 2004 (*triangles*), the *thick black line* is the power-law fit by Klug and Cashman (1996) for their data

of meters per second (e.g., 10–50 m/s at Soufrière Hills; Druitt et al. 2002) creating a delay between eruption initiation and fragmentation, which increases with depth in the conduit. We assume that an eruption's initiation is driven by gas overpressure beneath shallow, dense conduit magma. The release of this trapped gas ejects overlying conduit magma. Ejection of deeper conduit material is subsequently driven by exsolution and expansion of dissolved gas in response to a downward propagating decompression wave. For this reason, some water may have exsolved from breadcrust bombs after the onset of eruption, but prior to fragmentation of magma at depth (e.g., bombs with vesicular rinds). However, pre-fragmentation water contents are our closest approximation of pre-eruption conditions. Thus we use water contents preserved in the rinds of breadcrust bombs to infer pre-fragmentation storage conditions.

Equilibrium pressures determined from solubility relationships of H_2O and CO_2 for rhyolitic melts at 880°C (Newman and Lowenstern 2002) indicate that all erupted products were derived from fairly shallow levels in the conduit (Fig. 14). By morphologic type, preserved volatile contents constrain DB clasts to very low pressures ($P \leq 2.5$ MPa), FIB clasts to $2.5 \leq P < 10$ MPa, TkB clasts to $10 \leq P \leq 20$ MPa and TnB clasts to $15 < P \leq 69$ MPa. The pressure range determined for 880°C corresponds to a maximum of 2.8 km depth, based on 2,500 kg/m^3 magma density and an assumption of no overpressure in the conduit (Fig. 14). As typical Vulcanian eruptions require overpressures of approximately 10 MPa (Fagents and Wilson 1993; Morrissey and Mastin 2000), the actual maximum depth of origin may be closer to 2 km.

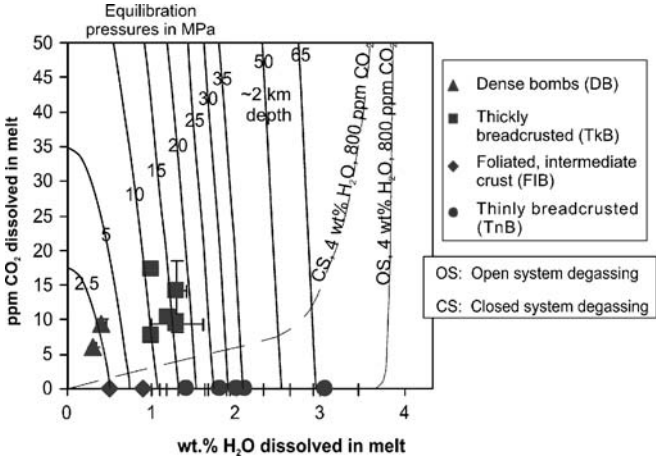

Fig. 14 Matrix glass water and carbon dioxide contents of ballistic bomb rinds. Equilibration pressures (shown in MPa) determined using solubility relationships of H_2O and CO_2 in rhyolitic melt at 880°C (Newman and Lowenstern 2002). Magmatic temperatures of 950 and 800°C increase and decrease estimated pressure by ~15% and ~13% respectively. Open and closed system degassing trends calculated for rhyolite melt at 880°C with listed starting composition using VolatileCalc (Newman and Lowenstern 2002), with starting volatile contents of 4 wt% water and 800 ppm CO_2 (Cioni FTIR data 2004, personal observations)

Pre-fragmentation CO_2 contents of 0–17 ppm do not significantly affect pressure estimates, although preservation of CO_2 at shallow levels raises questions about mechanisms of degassing. The volatile contents of matrix glass in, and rind vesicularity of, ballistic bombs at Guagua Pichincha are inconsistent with both open- and closed-system degassing models (Fig. 14) given trapped melt inclusion volatile contents of 4 wt% H_2O and 800 ppm CO_2 (Cioni FTIR data 2004, personal observations). CO_2 preserved in DB and TkB bomb rinds renders an open-system degassing model invalid, while the absence of CO_2 in TnB and FIB rinds appears to require open-system degassing. Chemical inconsistencies with degassing models are supported by physical evidence. A closed-system model requires that bubbles remain in contact with the melt from which they exsolved; such a model does not explain the absence of vesicles in TkB bomb rinds despite evidence for variable pre-eruptive degassing. On the other hand, the high vesicularity of TnB bomb rinds requires pre- and/or syn-eruptive vesiculation.

We propose two possible explanations for these data. First, magma that formed DB and TkB bombs may have experienced high gas fluxes at shallow levels, as recently suggested for small silicic eruptions (Rust et al. 2004). This model explains CO_2-H_2O trends such as those shown in Fig. 14 by continuous re-equilibration of magma with streaming vapor of constant composition, thus providing a source of observed CO_2 without requiring the physical presence of the original exsolved gas bubbles (i.e., a closed-system). In such a model, shallow magma loses gas (including all CO_2) until the conduit seals and gas escape is no longer possible (Fig. 14, open system degassing). Subsequent equilibration between vapor originating at depth (containing CO_2) and shallow melt would cause re-addition of CO_2 into shallow water-poor melt, as CO_2 is soluble at conduit pressures (Fig. 14, see equilibration pressure curves). Alternatively, high CO_2 concentrations could result from non-equilibrium open system degassing. With low enough bubble number densities or high enough decompression rates, Gonnermann and Manga (2005) find that degassing of CO_2 may occur under disequilibrium conditions, resulting in elevated CO_2/H_2O ratios. We prefer the first model; disequilibrium degassing should leave CO_2 in the glass of TnB bombs, which experienced, if anything, higher rates of decompression than DB and TkB bombs. Instead, the absence of CO_2 and moderate amount of H_2O not only indicates an open system, but also suggests that TnB magma was the source of the excess CO_2 preserved in TkB and DB magma. Alternatively, CO_2 may have been lost from TnB magma after fragmentation, but before ejection in to the atmosphere (i.e., while traveling through the conduit).

There are no published gas data from the Vulcanian eruptions at Pichincha. Initial COSPEC surveys did not show elevated SO_2 emission; however increased S concentrations in the Rio Azufrado during eruptive activity (Hall 2001) suggest that SO_2 was 'scrubbed' by the shallow groundwater system (J.-L. Le Pennec, 2004, personal communication), thus masking the degassing

behavior of Pichincha. For this reason, measurements were discontinued (P. Mothes, 2004, personal communication). We can extrapolate, however, from detailed observations of gas flux during and between Vulcanian eruptions of Galeras (Colombia) and Soufrière Hills (Montserrat) volcanoes (Stix et al. 1997; Edmonds et al. 2003). In both cases, a repeated pattern of SO_2 emission decreases preceding, and increases immediately following, explosions and dome-collapse events provide evidence of a conduit alternating between closed- and open-system behaviors. Variations in SO_2 emission rates have been ascribed to sealing of volcanic conduits prior to eruption and subsequent reopening of permeable gas pathways during explosive events, allowing upward migration of gas from deep magma that has vesiculated in response to evacuation of the overlying magma column. Consistent with this model, chemical evidence of gas fluxing is most pronounced in the products of consecutive eruptive episodes, for example the elevated CO_2 preserved in glassy products of pulsatory eruptions at Mono Craters (Newman et al. 1988; Rust et al. 2004) and the elevated ($^{210}Pb/^{226}Ra$) ratios in the products of the intermittent explosive eruptions of Mount St. Helens in 1980 (Berlo et al. 2004). We suggest that the elevated dissolved CO_2 in Guagua Pichincha breadcrust rinds provides evidence of similar high, transitory gas fluxes immediately following each Vulcanian eruption. The continuation of long period seismicity following each eruption (Fig. 2) may be evidence of this gas fluxing.

Model for Pichincha eruptions

The data presented above provide important constraints on the physical processes responsible for Vulcanian activity at Guagua Pichincha volcano in 1999. Constraints on pre-eruptive storage provided by eruption cyclicity and pre-fragmentation water and CO_2 contents inferred from glassy bomb rinds require (1) filling of the conduit and formation of a degassed plug, necessary for pressurization of the conduit, (2) evacuation of the conduit to a substantial depth (<2–2.8 km) during each eruption, and (3) immediate post-fragmentation degassing to explain the volatile data.

We first assemble a conduit stratigraphy to reconstruct pre-fragmentation storage conditions. Ballistic bombs with low H_2O contents, low vesicularities, and no breadcrusting (DB samples), originate from the shallowest levels of the conduit (Fig. 15, step 1). These blocks are found at the greatest distances from the vent, consistent with a low ejection angle anticipated for shallow conduit material. Bombs with higher H_2O, measurable CO_2, and thick glassy rinds (TkB samples) may represent magma that formed either just below DB magma or along the conduit margin; in either location post-explosion gas fluxes are likely to be high (Gonnermann and Manga 2003; Tuffen et al. 2003; Rust et al. 2004). Bombs with high H_2O and high rind vesicularities (TnB samples) originate from the deepest part of the evacuated conduit. It is difficult to place FIB bombs neatly into this stratigraphy due to their low water contents (intermediate between DB and TkB), lack of measurable CO_2, intermediate rim vesicularities and crack depths (between TkB and TnB), and absence of well-developed glassy rinds. However, macroscopic banding, microscopic evidence for bubble alignment, and enhanced permeability, all suggest that the samples are derived from locations of high shear (high velocity gradients), most likely along the conduit margins (e.g., Polacci et al. 2001). The stratigraphy depicted in Fig. 15 must develop during the repose interval (the time period between individual Vulcanian eruptions). Development of such a stratigraphy would involve vesiculation of ascending magma, loss of the exsolved volatile phase at shallow levels, and sealing of the shallow system to allow the pressurization required for the next eruption.

We attribute the cyclicity of eruptions at Guagua Pichincha volcano to repeated conduit filling, pressurization, and eruption, as suggested by Druitt et al. (2002) for Vulcanian eruptions at Soufrière Hills Volcano in 1997 (Fig. 15). An eruption is triggered when overpressure in the shallow conduit exceeds the strength of overlying degassed magma, causing rapid vesiculation of magma at depth in response to the ejection of overlying shallow conduit magma. When the decompression wave reached depths >~1.5–2.8 km (determined by maximum preserved H_2O contents), syn-eruptive depressurization was not sufficiently extensive or rapid to propel deep magma out of the conduit, but probably allowed vesiculation and permeability development. After each eruption, deeper magma ascended to form an extruding dome at the surface, resealing the top of the conduit and pressurizing the system again by gradual volatile exsolution from rising magma within the conduit (Fig. 15). Initial high gas fluxes into the upper conduit (e.g., Stix et al. 1997; Edmonds et al. 2003) could explain the presence of CO_2 in bombs from proto-DB and TkB magma.

A commonly invoked mechanism of conduit sealing is precipitation of hydrothermal minerals in the pore space near the conduit surface (e.g., Stix et al. 1997; Edmonds et al. 2003). This mechanism is, however, difficult to reconcile with the time scales of hours (Soufrière Hills Volcano, Montserrat) to days (Guagua Pichincha) between eruptions. Instead, we suggest that shallow filling of the conduit by slow magma ascent and re-pressurization of the conduit are related. Degassing of the uppermost magma and addition of crystals through degassing-induced crystallization would create a large density and viscosity contrast between the uppermost and deeper conduit magma (e.g., Sparks 1997; Cashman and Blundy 2000; Melnik and Sparks 2002). Additionally, the combination of lower viscosity and greater buoyancy of the deeper magma would cause it to ascend more rapidly than the shallow degassed magma. Also important may be the role of compressive stresses acting on the conduit walls in aiding upward migration of magma. Resultant compression of the uppermost magma cap caused both densification (through further gas loss) of the shallow magma and ‘quenching’ of the volatile signature (explaining CO_2 retention). Similar flow-induced degassing and densification might be expected

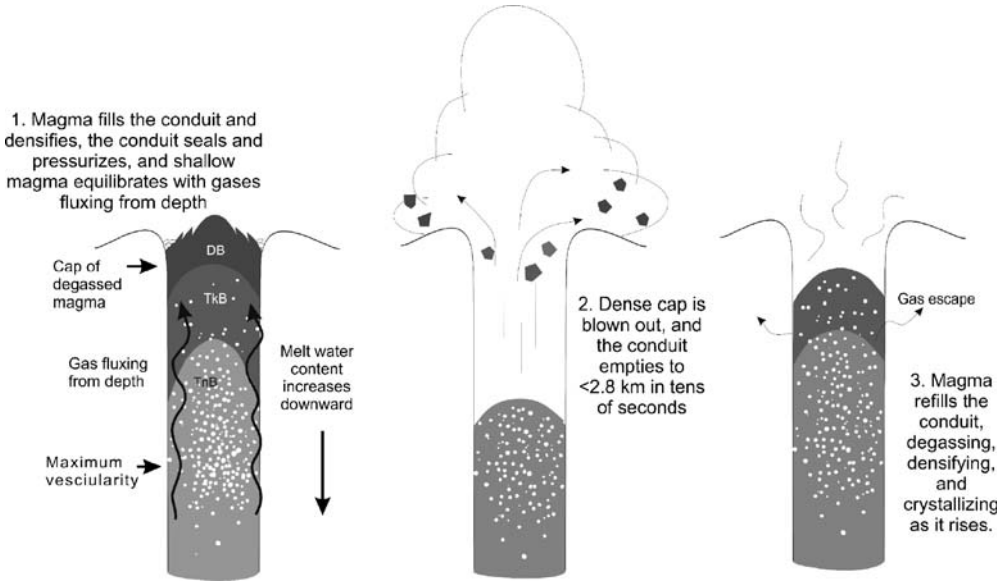

Fig. 15 Conduit stratigraphy from volatile contents and vesicularities of bomb samples. Eruption model for Pichincha volcano (Modified after model of 1997 eruptions of Soufrière volcano, Montserrat, Druitt et al. 2002)

along conduit walls (e.g., Newman et al. 1988; Rust et al. 2004). This model of conduit sealing is consistent with our inferences related to the pre-eruptive distribution of magma responsible for forming ballistic bombs with dense glassy rinds.

The repose interval between eruptions is linked to rates of magma ascent. Seismic data before the first eruption at Pichincha indicate an initial magma ascent rate of 6 cm/s for early subplinian activity (D. Villagomez, 2004, personal communication). That this rate is an overestimate of rates of magma rise during the Vulcanian episode is suggested by the observed change from subplinian to Vulcanian activity. Additionally, magma ascent rates of ~2 cm/s produced Vulcanian eruptions at Soufrière Hills Volcano, Montserrat (Druitt et al. 2002) that occurred with a repose interval of hours, rather than days. The longer repose intervals between Pichincha eruptions suggest even lower ascent rates than those at Montserrat. If the conduit at Pichincha were evacuated to ~2.8 km during each Vulcanian eruption, an ascent rate of 6 cm/s would allow the conduit to refill in ~12 h, a relatively short time when compared with the average repose interval of about one week. If the conduit refilled at a steady rate between eruptions, a minimum ascent rate of 0.5 cm/s is implied (2.8 km in 7 days). As refilling is probably followed by pressurization, we suggest that the actual rate of magma ascent lies between these values, but probably closer to the low end.

Conclusions

Breadcrust and dense ballistic bombs produced by a series of Vulcanian eruptions of Guagua Pichincha volcano, Ecuador, in 1999, provide insight into conduit processes that produce Vulcanian eruptions. First, we find that breadcrust bombs at Guagua Pichincha volcano form from shallow degassed magma and infer that low melt water contents cause delays in bubble nucleation. This model does not require the input of external water to quench breadcrust bomb rinds but does limit breadcrust bomb formation to shallow levels of the conduit (<2–2.8 km). Cycles of Vulcanian eruptions at Guagua Pichincha volcano involve repeated pressurization of the shallow, relatively degassed magma, which favors breadcrust bomb formation. Each eruption is preceded by ascent of magma to fill the conduit. Shallow melt undergoes open-system degassing through permeable conduit walls and the volcano surface. We suggest that post-eruption conduit sealing results from melt degassing, decompression-induced crystallization, and densification by input of magma from below, thus providing an alternative to previous models that require crack sealing by precipitation from hydrothermal fluids to pressurize the conduit. Magma rise and gas flux from below increase the pressure of gas trapped beneath an impermeable cap and extruding dome until a critical pressure is reached, resulting in explosive fragmentation of the magma, and not requiring interaction with external water. The cycle then repeats itself. Replenishment rates are broadly constrained to between 0.5 and 6 cm/s, consistent with estimates for Soufrière Hills Volcano, Montserrat.

Acknowledgements This work was funded by NSF grants EAR-0207362 and EAR-0510437 to Cashman. We would like to thank M. Hall and P. Mothes for thoughtful discussions of the 1999–2000 activity at Guagua Pichincha while we were performing fieldwork. Discussions with D. Villagomez and J.-L. LePennec added details to complement critical interpretations of the data. P. Wallace kindly provided guidance for FTIR analyses. We would also like to thank A. Rust, J. White and two anonymous reviewers for reviews that helped us to clarify our assumptions and interpretations.

Appendix

Total accommodation of interior expansion by exterior cracking (such that cracks propagate only as deep as the dense outer rind):

$$\frac{volume\ of\ cracks}{volume\ of\ vesicles} = \frac{\left(r_i\left(\frac{1}{1-\Delta\phi}\right)^{\frac{1}{3}} + t_r\right)^3 - \frac{r_i^3}{(1-\Delta\phi)} - (r_i + t_r)^3 + r_i^3}{r_i^3\left(\frac{\Delta\phi}{1-\Delta\phi}\right)}$$

where r_i = radius of interior (pre-expansion), t_r = thickness of rind, and $\Delta\phi=\phi_b-\phi_r$. For a bomb with 75% of the interior vesiculating to 60% (r_i=3, t_r=1, and $\Delta\phi$=0.6):

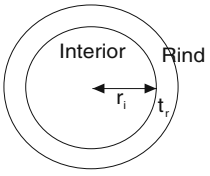

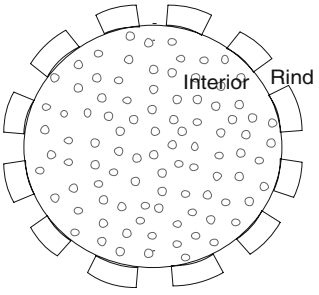

$$\frac{volume\ of\ cracks}{volume\ of\ vesicles} = 0.64.$$

References

Arciniega-Ceballos A, Chouet BA, Dawson P (1999) Very long-period signals associated with vulcanian explosions at Popocatepetl Volcano, Mexico. Geophys Res Lett 26:3013–3016

Barberi F, Ghigliotti M, Macedonio G, Orellana H, Pareschi MT, Rosi M (1992) Volcanic hazard assessment of Guagua Pichincha (Ecuador) based on past behaviour and numerical models. J Volcanol Geotherm Res 49:53–68

Barmin A, Melnik O, Sparks RSJ (2002) Periodic behavior in lava dome eruptions. Earth Planet Sci Lett 199:173–184

Behrens H, Tamic N (2004) Determination of the molar absorption coefficient for the infrared absorption band of CO_2 in rhyolitic glasses. Am Mineral 89:301–306

Berlo K, Blundy J, Turner S, Cashman K, Hawkesworth C, Black S (2004) Geochemical precursors to volcanic activity at Mount St. Helens, USA. Science 306:1167–1169

Capra L, Macias JL, Espindola JM, Siebe C (1998) Holocene plinian eruption of La Virgen volcano, Baja California, Mexico. J Volcanol Geotherm Res 80:239–266

Cashman KV, Blundy J (2000) Degassing and crystallization of ascending andesite and dacite. Phil Trans R Soc Lond 358:1487–1513

Cashman KV, Sturtevant B, Papale P, Navon O (2000) Magmatic fragmentation. In: Sigurdsson H (ed) Encyclopedia of volcanoes. Academic Press, San Diego, pp 421–430

Chouet BA, Page RA, Stephens CD, Lahr JC, Power JA (1994) Precursory swarms of long-period events at Redoubt Volcano (1989–1990), Alaska: their origin and use as a forecasting tool. J Volcanol Geotherm Res 62:95–135

Clarke AB, Neri A, Voight B, Macedonio G, Druitt TH (2002) Computational modelling of the transient dynamics of the August 1997 Vulcanian explosions at Soufrière Hills Volcano, Montserrat: influence of initial conduit conditions on near-vent pyroclastic dispersal. In: Druitt TH, Kokelaar BP (eds) The eruption of Soufrière Hills Volcano, Montserrat, from 1995 to 1999. Geol Soc London Mem 21:319–348

Cruz GG, Chouet BA (1997) Long-period events, the most characteristic seismicity accompanying the emplacement and extrusion of a lava dome in Galeras Volcano, Colombia, in 1991. J Volcanol Geotherm Res 77:121–158

Druitt TH, Young SR, Baptie B, Bonadonna C, Calder ES, Clarke AB, Cole PD, Harford CL, Herd RA, Luckett R, Ryan G, Voight B (2002) Episodes of cyclic Vulcanian explosive activity with fountain collapse at Soufrière Hills Volcano, Montserrat. In: Druitt TH, Kokelaar BP (eds) The eruption of Soufrière Hills Volcano, Montserrat, from 1995 to 1999. Geol Soc London Mem 21:281–306

Edmonds M, Oppenheimer C, Pyle DM, Herd RA, Thompson G (2003) SO_2 emissions from Soufriere Hills Volcano and their relationship to conduit permeability, hydrothermal interactions and degassing regime. J Volcanol Geotherm Res 124:23–43

Eichelberger JC, Carrigan CR, Westrich HR, Price RH (1986) Non-explosive silicic volcanism. Nature 323:598-602

Fagents SA, Wilson L (1993) Explosive volcanic eruption-VII. The ranges of pyroclasts ejected in transient volcanic explosions. Geophys J Int 113:359–370

Fisher RV, Schmincke H-U (1984) Pyroclastic rocks. Springer, Berlin Heidelberg New York

Formenti Y, Druitt TH, Kelfoun K (2003) Characterisation of the 1997 Vulcanian explosions of Soufrière Hills Volcano, Montserrat, by video analysis. Bull Volcanol 65:587–605

Francis P (1993) Volcanoes: a planetary perspective. Oxford University Press, Oxford

Friedman I, Smith RL, Long WD (1966) Hydration of natural glass and formation of perlite. Geol Soc Am Bull 77:323–327

Fudali RF, Melson WG (1972) Ejecta velocities, magma chamber pressure and kinetic energy associated with the 1968 eruption of Arenal Volcano. Bull Volcanol 35:383–401

Gonnermann HM, Manga M (2003) Explosive volcanism may not be an inevitable consequence of magma fragmentation. Nature 426:432–435

Gonnermann HM, Manga M (2005) Non-equilibrium magma degassing: Results from modeling of the ca. 1340 A.D. eruption of Mono Craters, California. Earth Planet Sci Lett 238:1–16

Hall M (2001) Guagua Pichincha. In: GVN: Bull Global Volcan Network. http://volcano.si.edu/world/ Cited 30 July 2001

Hammer JE, Cashman KV, Hoblitt RP, Newman S (1999) Degassing and microlite crystallization during pre-climactic events of the 1991 eruption of Mt. Pinatubo, Philippines. Bull Volcanol 60:355–380

Harford CL, Sparks RSJ, Fallick AE (2003) Degassing at the Soufrière Hills Volcano, Montserrat, recorded in matrix glass compositions. J Petrol 8:1503–1523

Hoblitt RP, Harmon RS (1993) Bimodal density distribution of cryptodome dacite from the 1980 eruption of Mount St. Helens, Washington. Bull Volcanol 55:421–437

Innocentini MDM, Pandolfelli VC (2001) Permeability of porous ceramics considering the Klinkenberg and inertial effects. J Amer Ceram Soc 84:941–944

Johnson DM, Hooper PR, Conrey RM (1999) XRF analysis of rocks and minerals for major and trace element analysis on a single low dilution Litetraborate fused bead. Adv X-ray Anal 41:843-867

Klug C, Cashman KV (1996) Permeability development in vesiculating magmas: implications for fragmentation. Bull Volcanol 58:87–100

Klug C, Cashman KV, Bacon CR (2002) Structure and physical characteristics of pumice from the climactic eruption of Mount Mazama (Crater Lake), Oregon. Bull Volcanol 64:486–501

Kuntz MA, Rowley PD, MacLeod NS, Reynolds RL, McBroome LA, Kaplan AM, Lidke DJ (1981) Petrography and particle-size distribution of pyroclastic-flow, ash-cloud, and surge deposits. In: Lipman P, Mullineaux DR (eds) The 1980 eruptions of Mount St Helens, Washington. United States Government Publishing Office, Washington, DC, pp 525–540

Mastin LG (2001) Eject! A simple calculator of ballistic trajectories for blocks ejected during volcanic eruptions. USGS Open-File Report 01-45, USGS, Reston, VA

Melnik O, Sparks RSJ (2002) Modelling of conduit flow dynamics during explosive activity at Soufrière Hills Volcano, Montserrat. In: Druitt TH, Kokelaar BP (eds) The eruption of Soufrière Hills Volcano, Montserrat, from 1995 to 1999. Geol Soc London Mem 21:307–317

Melson WG, Saenz R (1974) Volume, energy and cyclicity of eruptions of Arenal Volcano, Costa Rica. Bull Volcanol 37:416–437

Morrissey MM, Mastin LG (2000) Vulcanian eruptions. In: Sigurdsson H (ed) Encyclopedia of volcanoes. Academic Press, San Diego, pp 463–475

Müller G (1998) Starch columns: analog model for basalt columns. J Geophys Res 103:15239–15253

Nairn IA, Self S (1978) Explosive eruptions and pyroclastic avalanches from Ngaurahoe in February 1975. J Volcanol Geotherm Res 3:39–60

Nakada S, Motomura Y, Shimuzu H (1995) Manner of magma ascent at Unzen Volcano (Japan). Geophys Res Lett 22:567–570

Newman S, Lowenstern JB (2002) VolatileCalc: a silicate melt-H_2O-CO_2 solution model written in Visual Basic for EXCEL. Comput Geosci 28:597–604

Newman S, Epstein S, Stolper E (1988) Water, carbon dioxide, and hydrogen isotopes in glasses from the CA. 1340 A.D. eruption of the Mono Craters, California: constraints on degassing phenomena and initial volatile content. J Volcanol Geotherm Res 35:75–96

Polacci M, Papale P, Rosi M (2001) Textural heterogeneities in pumices from the climactic eruption of Mount Pinatubo, 15 June 1991, and implications for magma ascent dynamics. Bull Volcanol 63:83–97

Rust AC, Cashman KV (2004) Permeability of vesicular silicic magma: inertial and hysteresis effects. Earth Planet Sci Lett 228:93–107

Rust AC, Cashman KV, Wallace PJ (2004) Magma degassing buffered by vapor flow through brecciated conduit margins. Geology 32:349–352

Schmincke H-U, Bogaard PVD, Freundt A (1990) Quaternary Eifel Volcanism. IAVCEI International Volcanological Congress, September 1990, Mainz (FRG), Workshop on Explosive Volcanism 186

Self S, Wilson L, Nairn IA (1979) Vulcanian eruption mechanisms. Nature 277:440–443

Sowerby J, Keppler H (1999) Water speciation in rhyolitic melt determined by in-situ infrared spectroscopy. Am Mineral 84:1843–1849

Sparks RSJ (1997) Causes and consequences of pressurisation in lava dome eruptions. Earth Planet Sci Lett 150:177–189

Spera FJ (2000) Physical properties of magma. In: Sigurdsson H, Houghton BF, McNutt SR, Rymer H, Stix J (eds) Encyclopedia of volcanoes. Academic Press, San Diego, pp 171–190

Stix J, Torres RC, Narvaez LM, Cortes JGP, Raigosa AJ, Gomez DM, Castonguay R (1997) A model of vulcanian eruptions at Galeras volcano, Colombia. J Volcanol Geotherm Res 77:285–303

Thomas N, Jaupart C, Vergniolle S (1994) On the vesicularity of pumice. J Geophys Res 99:15633–15644

Thomas RME, Sparks RSJ (1992) Cooling of tephra during fallout from eruption columns. Bull Volcanol 54:542–553

Toramaru A, Matsumoto T (2004) Columnar joint morphology and cooling rate: a starch-water mixture experiment. J Geophys Res 109:B02205. DOI 02210.01029/02003JB002686

Tuffen H, Dingwell DB, Pinkerton H (2003) Repeated fracture and healing of silicic magma generates flow banding and earthquakes? Geology 31:1089–1092

Turcotte DL, Ockendon H, Ockendon JR, Cowley SJ (1990) A mathematical model of vulcanian eruptions. Geophys J Int 103:211–217

Villagomez D (2000) Sismicidad del volcan Guagua Pichincha, 1998–1999. Escuela Politecnica Nacional, Quito, Ecuador

Vougioukalakis G (1995) Santorini "The Volcano". Institute for the study and monitoring of the Santorini volcano, Firostefani, Santorini, Greece

Walker G (1969) The breaking of magma. Geol Mag 106:166–173

Walker G (1982) Eruptions of andesitic volcanoes. In: Thorpe RS (ed) Andesites: orogenic andesites and related rocks. Wiley, New York, pp 403–413

Woods AW (1995) A model of vulcanian explosions. Nucl Eng Des 155:345–357

Yamagishi H, Feebrey C (1994) Ballistic ejecta from the 1988-1989 andesitic Vulcanian eruptions of Tokachidake volcano, Japan: morphological features and genesis. J Volcanol Geotherm Res 59:269–278

Zhang Y, Belcher R, Ihinger PD, Wang L, Xu Z, Newman S (1997) New calibration of infrared measurement of dissolved water in rhyolitic glasses. Geochim Cosmochim Acta 61:3089–3100